Body MRI: Imaging Protocols, Techniques, and Lessons Learned

Anup S. Shetty, MD
Tyler J. Fraum, MD
Daniel R. Ludwig, MD
Mark J. Hoegger, MD, PhD
Maria Zulfiqar, MD
David H. Ballard, MD
Benjamin S. Strnad, MD
Mohamed Z. Rajput, MD
Malak Itani, MD
Reza Salari, MD
Michael H. Lanier, MD
Vincent M. Mellnick, MD

Abbreviations: ADC = apparent diffusion coefficient, AML = angiomyolipoma, APHE = arterial phase hyperenhancement, DWI = diffusion-weighted imaging, HBP = hepatobiliary phase, HCC = hepatocellular carcinoma, LI-RADS = Liver Imaging Reporting and Data System, TE = echo time, 3D = three dimensional, THID = transient hepatic intensity difference

RadioGraphics 2022; 42:2054–2074

https://doi.org/10.1148/rg.220025

Content Codes: GI GU MR

From the Mallinckrodt Institute of Radiology, Washington University School of Medicine, 510 S Kingshighway Blvd, Campus Box 8131, St Louis, MO 63110. Presented as an education exhibit at the 2021 RSNA Annual Meeting. Received February 8, 2022; revision requested March 22 and received March 29; accepted April 5. For this journal-based SA-CME activity, the authors T.J.F. and D.H.B. have provided disclosures (see end of article); all other authors, the editor, and the reviewers have disclosed no relevant relationships. **Address correspondence to** A.S.S. (email: *anup.shetty@wustl.edu*).

SA-CME LEARNING OBJECTIVES

After completing this journal-based SA-CME activity, participants will be able to:

- Discuss a logical approach to selecting an appropriate MRI contrast agent for liver imaging on the basis of indication and patient factors.
- Modify a body MRI protocol to use Dixon chemical shift imaging and various techniques to address motion artifact.
- Describe how to use DWI in an abdominal approach as a tool for greater lesion conspicuity and problem solving.

See rsna.org/learning-center-rg.

Body MRI has evolved from a niche subspecialty to a standard modality in the practice of abdominal radiology. However, the practicing radiologist may feel uncomfortable interpreting body MRI studies owing to a lack of case volume and inconsistent exposure. The authors highlight teaching points and subtleties central to better acquisition and interpretation of body MRI studies. Appropriate contrast agent selection and arterial phase acquisition timing provide greater diagnostic certainty in answering common clinical questions at liver MRI, such as assessing cirrhosis and evaluating focal liver lesions. Clinically relevant artifacts and physiologic phenomena, such as magnetic susceptibility and transient hepatic intensity difference, must be recognized and appropriately used when reading a study. Fat within organs and lesions is commonly encountered at body MRI. The authors discuss the nuances of common and uncommon entities, how to address fat suppression failure, assessment of bone marrow at body MRI, and an organized approach to fat-containing renal and adrenal masses. Motion artifacts are more commonly encountered at body MRI than at MRI of other anatomic regions, and understanding the various techniques, their benefits, and trade-offs will aid the body imager in protocol design and moving beyond "nondiagnostic" examinations. Challenging anatomic sites to evaluate at body MRI are reviewed. Finally, the authors offer tips for accurate interpretation of diffusion-weighted imaging, hepatobiliary phase imaging, and posttreatment imaging studies. By reviewing this article, the abdominal imager will be better prepared to perform and interpret body MRI studies confidently and accurately.

An invited commentary by Kalb is available online.
Online supplemental material is available for this article.

Introduction

Body MRI is a cornerstone of abdominal imaging and a key tool for problem solving, diagnosis, monitoring of treatment response, and surveillance. More so than musculoskeletal and brain MRI, body MRI is confounded by protocols of varying design and quality (1). Artifacts related to motion and speed of acquisition are common and must be considered in the context of both individual MRI scanner capabilities and individual patient anatomy. Timing of image acquisition, including dynamic acquisitions with intravenous gadolinium-based contrast agents and sequence ordering within protocols, greatly impacts the quality and diagnostic utility of body MRI. Newer techniques in body MRI to image fat and address motion may be unfamiliar to the practicing body imager and therefore underutilized. Interpretation of diffusion-weighted imaging (DWI), hepatobiliary phase (HBP) imaging, and posttreatment imaging studies often requires special consideration and must be approached thoughtfully.

TEACHING POINTS

- In patients with risk factors for primary liver malignancy (eg, cirrhosis), arterial phase quality is critical. The LI-RADS strongly emphasizes the acquisition of postcontrast T1-weighted late hepatic arterial phase images to identify APHE, a major feature of HCC and a mandatory feature for characterization as LI-RADS 5 (definitely HCC).
- T2-weighted imaging can usually be performed after contrast agent administration without significantly altering the appearance of the abdominal organs, as contrast agents shorten T2 much less than T1. The major exception is the urinary tract, where concentrated gadolinium may shorten T2 sufficiently to obscure potential findings.
- Diffuse hepatic steatosis is commonly diagnosed by observing diffuse signal loss on opposed-phase images compared with in-phase images. Less commonly, steatosis may be nodular, focal, and infiltrative, requiring careful attention to chemical shift imaging.
- Motion artifact attributable to respiratory motion is the most common cause of a nondiagnostic or suboptimal body MRI examination. These artifacts can be mitigated by increasing acquisition speed to shorten breath holds, using motion-insensitive acquisition techniques, or utilizing respiratory triggering.
- DWI often provides the greatest lesion conspicuity of any noncontrast sequence in a body MRI protocol. However, diffusion restriction should not be equated with malignancy, as both benign and malignant entities can restrict diffusion.

The purpose of this article is to provide a tool kit for the body MR imager to hone their imaging protocols, identify and leverage common artifacts, detect and use fat effectively in diagnosis, address motion artifacts prospectively, recognize common blind spots and pain points, and identify subtle findings that impact interpretation. Cases harnessing our experience with these topics illustrate key learning points. We describe lessons we have learned over time that empower radiologists to interpret body MRI studies with more confidence and accuracy.

Imaging Protocols and Contrast Agents

Liver MRI Contrast Agent Selection

The choice of a gadolinium-based contrast agent for liver MRI should be predicated on specific patient characteristics, the pretest probability of malignancy versus benignity, and the clinical question to be answered (Table) (2). In patients with risk factors for primary liver malignancy (eg, cirrhosis), arterial phase quality is critical. The Liver Imaging and Reporting Data System (LI-RADS) strongly emphasizes the acquisition of postcontrast T1-weighted late hepatic arterial phase images to identify arterial phase hyperenhancement (APHE), a major feature of hepatocellular carcinoma (HCC) and a mandatory feature for characterization as LI-RADS 5 (definitely HCC) (3). The timing and degree of enhancement are paramount for distinguishing between nonrim and rim APHE. Extracellular contrast agents (Table) provide high-quality arterial phase imaging with optimal enhancement (typically greater than gadoxetate disodium [Eovist; Bayer]) without transient arterial phase motion, which occurs in up to 10%–20% of examinations with gadoxetate (Fig 1) (4,5). Extracellular agents also provide multiple opportunities to identify washout (ie, portal venous phase onward); by comparison, washout can be identified in only the portal venous phase at gadoxetate examinations owing to rapid hepatocyte uptake (3). Gadoxetate does allow assessment of additional LI-RADS M (malignancy, not definitely HCC) features, such as transitional phase or HBP targetoid appearance, but at the expense of potential arterial phase motion leading to inability to define a continuous rim of APHE.

In patients without cirrhosis, the next consideration is the pretest probability of a focal liver lesion (FLL) representing metastasis from an extrahepatic primary malignancy versus a benign lesion such as a hemangioma, adenoma, or focal nodular hyperplasia. Imaging hemangiomas can be problematic with gadoxetate, as progressive centripetal enhancement may not be present in the later postcontrast phases owing to hepatocyte uptake resulting in blood pool clearance (Fig 2) (6). In patients with known malignancy and prior CT or MRI examinations without possible hemangioma, gadoxetate should be preferred, offering greater sensitivity for detecting small metastases (7). If no prior imaging examination is available or if a hemangioma is possible based on findings at prior imaging, an extracellular agent may facilitate hemangioma diagnosis, with a concurrent decrease in sensitivity for small metastases.

In patients without known or suspected malignancy in which characterization of an FLL is requested, gadobenate dimeglumine (MultiHance; Bracco) is of potential value. Gadobenate combines the behavior of a pure extracellular contrast agent during dynamic imaging (ie, hemangiomas will enhance centripetally) with an HBP at 1 hour after injection that helps differentiate focal nodular hyperplasia from hepatic adenoma (8). However, the drawback of a longer delay for HBP imaging with gadobenate (60 minutes) compared with gadoxetate (20 minutes) can create potential workflow challenges.

Liver MRI Contrast Agent Timing

Optimizing the arterial phase timing is critical in detecting APHE in the cirrhotic liver. The hepatic arterial phase can be divided into the early phase,

Contrast Agents for Liver MRI

Contrast Agent Name	Trade Name	Class	Benefits	Drawbacks
Gadopentetate dimeglumine	Magnevist (Schering)	Extracellular	No increased risk of arterial phase motion	No HBP
Gadoterate meglumine	Dotarem (Guerbet), Clariscan (GE Healthcare)	Extracellular	No increased risk of arterial phase motion	No HBP
Gadodiamide	Omniscan (GE Healthcare)	Extracellular	No increased risk of arterial phase motion	No HBP
Gadoteridol	ProHance (Bracco)	Extracellular	No increased risk of arterial phase motion	No HBP
Gadobutrol	Gadavist (Bayer)	Extracellular	No increased risk of arterial phase motion	No HBP
Gadobenate dimeglumine	MultiHance (Bracco)	Extracellular, hepatobiliary	No increased risk of arterial phase motion Dynamic liver imaging appearance similar to other extracellular agents HBP	Longer delay for HBP (at least 60 minutes)
Gadoxetate	Primovist (Bayer), Eovist (Bayer)	Hepatobiliary	HBP with shorter delay (20 minutes) and greater contrast than with gadobenate	Risk for arterial phase motion (10%–20%) Dynamic liver enhancement different than that with extracellular agents Potentially weaker arterial phase enhancement

with no portal vein enhancement, and the late phase, with submaximal portal vein enhancement (ie, less hyperintense than with the portal venous phase) (Fig 3). Notably, some HCCs will exhibit APHE only in the late hepatic arterial phase (3). A fixed delay from injection to acquisition (eg, 20–25 seconds) is simple but unreliable for capturing the late arterial phase, which varies among patients or even between examinations for an individual patient. Alternatively, bolus tracking is widely available on newer scanners and involves placing a region of interest on the descending thoracic or abdominal aorta, which is dynamically imaged during contrast agent bolus injection. Once a threshold signal intensity is reached, image acquisition commences (9). On older scanners without bolus tracking, scan timing can be calculated by using a test bolus by injecting 1 mL of contrast agent during a dynamic acquisition through the abdominal aorta to determine the time to peak enhancement (TTP). The delay from full bolus injection to start of image acquisition can then be calculated by the technologist by using the following equation:

$$\text{Delay} = \text{TTP} + \frac{\text{injection duration}}{2} - T_{\text{kspace}} + 5 \text{ seconds},$$

where T_{kspace} is time to center of k-space. The value of 5 seconds is a "fudge factor" to account for the delay from peak enhancement of the abdominal aorta to the start of portal venous inflow in the late hepatic arterial phase (9).

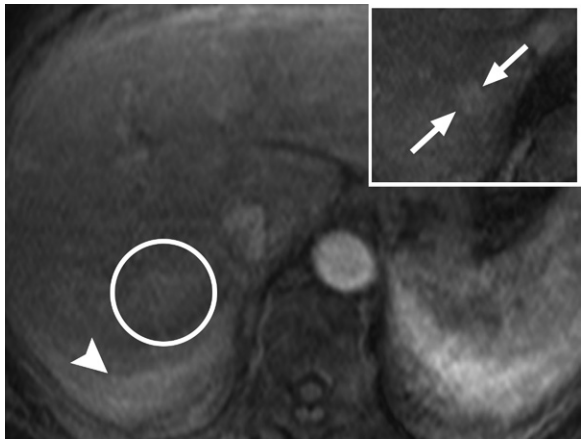

Figure 1. Transient arterial phase motion seen with use of gadoxetate contrast agent in a 64-year-old woman. Axial T1-weighted arterial phase MR image is degraded by respiratory motion artifact (arrowhead), creating ambiguity as to whether nonrim APHE in a segment VII observation (circle) is truly present. Image from a repeat examination with an extracellular agent (inset) confirms nonrim APHE (arrows) in a LI-RADS 5 HCC.

On the newest scanners, two additional techniques are available, both involving multiple

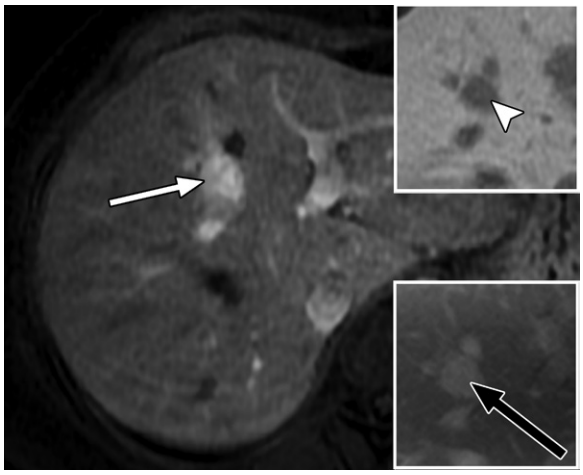

Figure 2. Contrast enhancement of a hemangioma with gadoxetate and an extracellular contrast agent in a 33-year-old woman. Axial T1-weighted arterial phase MR image shows hyperenhancement (white arrow) of a segment VIII liver lesion similar to that of the venous blood pool. With gadoxetate, the transitional phase image obtained 5 minutes after contrast agent administration (top right inset) shows hypoenhancement of the lesion (arrowhead). MR image from a repeat examination with an extracellular agent (bottom right inset) shows persistent enhancement at 5 minutes after contrast agent administration similar to that of the venous blood pool, confirming the diagnosis of a flash-filling hepatic hemangioma.

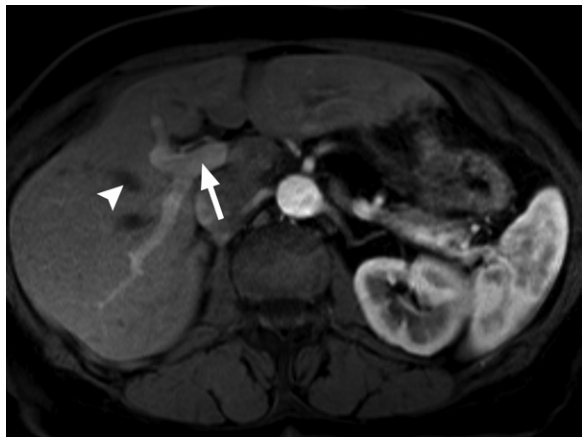

Figure 3. Late hepatic arterial phase timing of postcontrast T1-weighted liver MRI. Axial MR image in the late hepatic arterial phase shows that the portal vein (arrow) is submaximally enhanced, with no contrast enhancement of the hepatic veins (arrowhead). The timing of this acquisition is variable from patient to patient and examination to examination and can be achieved with various methods.

acquisitions during the hepatic arterial phase. The first technique uses time-resolved imaging with k-space sharing or "keyhole imaging" (eg, Time-resolved angiography With Interweaved Stochastic Trajectories [TWIST; Siemens], Time-Resolved Imaging of Contrast KineticS [TRICKS; GE]), in which the center of k-space (the "keyhole," where contrast information resides) is repeatedly sampled during a breath-hold acquisition to produce images at multiple arterial phase time points (10) (Fig E1). The periphery of k-space, which provides the spatial resolution data that do not change significantly during contrast agent bolus injection, is sampled much less frequently and shared across multiple central k-space samples. This approach significantly shortens the acquisition time for each contrast phase, resulting in higher temporal resolutions. This technique aims to maximize the likelihood that the late arterial phase is captured, at the expense of lower signal-to-noise ratio (SNR) and more images to review during interpretation. If respiratory motion occurs during acquisition, the artifact is "shared" across all views.

An alternative approach is to use a free-breathing sequence in which image data are acquired continuously before, during, and following contrast agent bolus injection (spanning 3–5 minutes). These sequences use compressed sensing to facilitate undersampling of data acquired by using a golden radial angle spoke trajectory (GRASP), followed by wavelet transformation to a sparse projection and iterative reconstruction (GRASP-VIBE [Siemens], HyperSENSE [GE], compressed SENSE [Philips]) (11,12) (Fig E2). The data from these continuous acquisitions can be retrospectively binned according to user preference to improve temporal resolution (shorter time periods used for reconstruction) or SNR (longer time periods). Respiratory phase binning is also performed to reduce motion artifact. We reconstruct a precontrast phase, three arterial phases, a portal venous phase, and a delayed phase. Additional drawbacks of this technique, which is available on only the newest scanner platforms, include long reconstruction times, larger datasets, and radial streak artifacts.

Protocol Modifications

T2-weighted imaging can usually be performed after contrast agent administration without significantly altering the appearance of the abdominal organs, as contrast agents shorten T2 much less than T1 (13). The major exception is the urinary tract, where concentrated gadolinium may shorten T2 sufficiently to obscure potential findings (14). This is particularly important in bladder or urography protocols, where T2-weighted imaging and DWI of the collecting systems and bladder should be performed before contrast agent administration (Fig 4). If short-τ inversion recovery (STIR) is used for fat suppression, the sequence should be performed before contrast agent administration, as gadolinium can shorten the T1 of a normal organ or lesion to the T1 of fat (~250 msec at 1.5 T), inadvertently suppressing its signal (Fig 5) (15).

Careful sequence placement within a protocol can also reduce examination length. For example, gadoxetate protocols will include a HBP at 20 minutes after injection. The contrast agent should be administered as early as possible in the protocol to begin the 20-minute clock, with T2-weighted imaging and DWI moved between dynamic contrast imaging and the HBP to use the "dead space" most efficiently (16). Consequently, these T2-weighted images should use non-STIR techniques for fat suppression. An easily overlooked facet of gadoxetate use in two-station abdomen and pelvis protocols is that postcontrast imaging of the pelvis should be performed as rapidly as possible after abdominal dynamic imaging, when some contrast material has not yet been cleared from the blood pool by hepatocytes. Failure to do so can result in suboptimal enhancement of pelvic structures (Fig E3).

Medications administered for an imaging protocol, such as glucagon for enterography, have a limited span of effect (17). Motion-sensitive sequences, such as dynamic T1-weighted bowel sequences, should be performed soon after medication administration for maximal reduction in motion artifact (Fig E4). Less motion-sensitive sequences, such as single-shot T2-weighted and free-breathing DWI sequences, can be performed later without significant loss of quality.

Gadoxetate

Several factors affecting the quality of liver imaging with gadoxetate should be considered in protocol design and selection. Transient arterial phase motion can adversely affect detection of arterially hyperenhancing metastases from neuroendocrine neoplasms or melanoma, but the benefit of greater sensitivity in the HBP for small metastases likely outweighs this drawback (Fig 6). Adjusting the flip angle of the spoiled three-dimensional (3D) T1-weighted gradient-echo acquisition for the HBP enhances diagnostic yield by improving contrast between hyperintense liver parenchyma and metastases owing to the shorter T1 of liver parenchyma in the HBP after contrast agent uptake. The flip angle should be increased from the standard 9°–12° for dynamic imaging to 35°–40° for the HBP (Fig 7) (18). HBP liver signal intensity is adversely affected by liver dysfunction and hyperbilirubinemia, as gadoxetate uptake is mediated by the same transporter as bilirubin (19). A total bilirubin threshold of 3 mg/dL is reasonable to determine whether a gadoxetate HBP will be beneficial, although some patients with liver dysfunction but normal bilirubin levels will likewise exhibit poor gadoxetate uptake (Fig 8). Finally, if there is concern for bile leak, the HBP acquisition should instead be obtained at 60–90 minutes after injection to enhance sensitivity, particularly in patients with underlying liver dysfunction (Fig 9) (20). For patients who are too unstable to remain in the MRI department for that duration, we have occasionally injected gadoxetate in the intensive care unit ahead of a planned imaging session, with an additional dose of an extracellular agent given for dynamic imaging if needed.

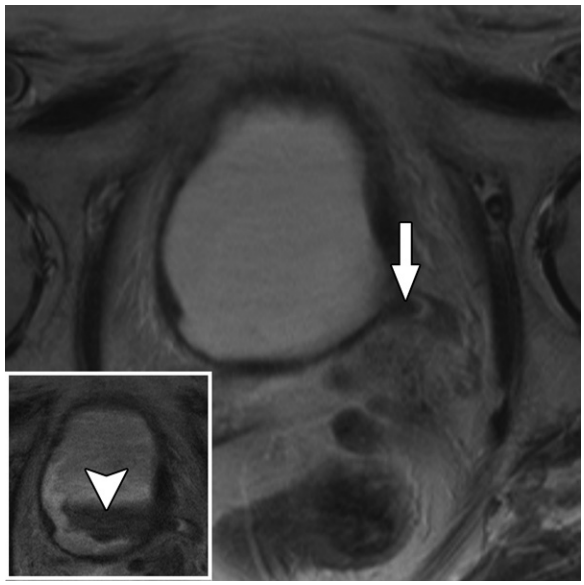

Figure 4. Pre- and postcontrast T2-weighted imaging of the bladder in an 87-year-old man undergoing MRI of the abdomen and pelvis. Axial T2-weighted MR image shows a left ureteral filling defect (arrow), which may be mistaken on a postcontrast T2-weighted image (inset) for excretion of concentrated gadolinium (arrowhead) into the bladder. In a bladder protocol, T2-weighted imaging should be performed before the administration of a contrast agent.

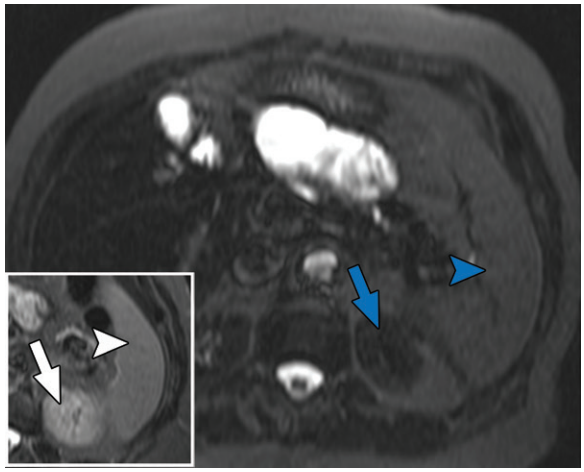

Figure 5. Pre- and postcontrast STIR sequences at abdominal MRI in a 76-year-old woman. STIR relies on T1 and an appropriately selected inversion time to reduce fat signal intensity. If a postcontrast STIR sequence is performed, as demonstrated on the axial MR image, the spleen (blue arrowhead) and kidney (blue arrow) will have reduced signal intensity owing to the T1-shortening effects of gadolinium compared with their normal signal intensity on the axial precontrast STIR image (inset). STIR sequences should be performed only before contrast agent administration.

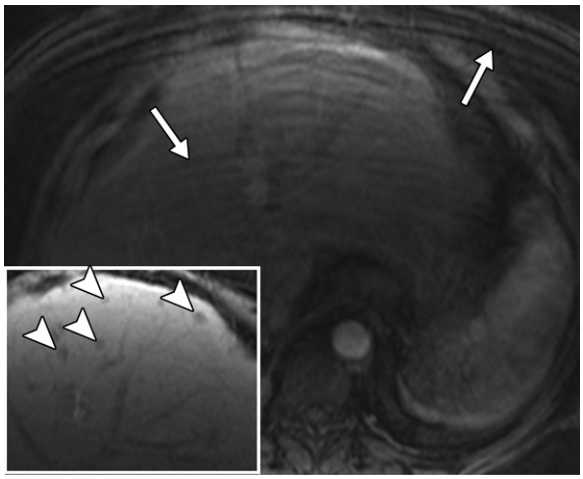

Figure 6. Trade-offs in imaging hypervascular metastases with gadoxetate in a 59-year-old woman with metastatic melanoma. Axial MR image in the arterial phase is markedly degraded by transient arterial phase motion (arrows), limiting the evaluation of hyperenhancing metastases. However, the HBP image (inset) clearly shows numerous hypointense liver metastases (arrowheads). We prefer gadoxetate as the contrast agent for liver MRI in patients with hypervascular metastases.

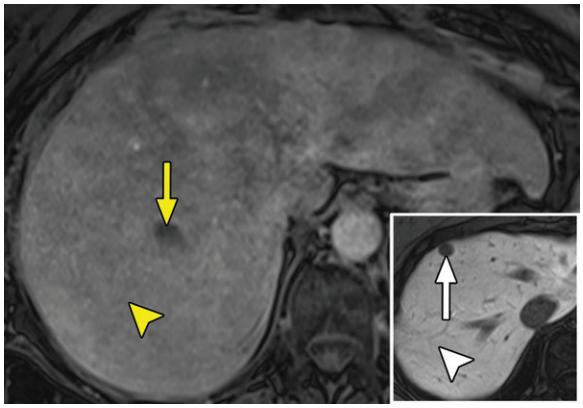

Figure 7. Effects of flip angle on background liver hyperintensity with gadoxetate-enhanced HBP imaging in two different patients. Axial 3D T1-weighted spoiled gradient-echo MR image shows that using a standard flip angle of 10° results in less hyperintensity of background liver (yellow arrowhead) and less contrast between normal liver and a hypointense mass (yellow arrow) compared with a flip angle of 35° (inset), which optimizes contrast between background liver (white arrowhead) and a hypointense mass (white arrow).

Dixon Chemical Shift Imaging

As a fundamental component of a body MRI protocol, dual-echo chemical shift imaging includes multiple acquisitions with progressively longer echo times (TEs). These TEs are selected to coincide with times when the magnetic dipoles of water and fat protons, which precess at slightly different Larmor frequencies, are parallel (ie, in phase) or antiparallel (ie, opposed phase). Signal loss between in-phase and opposed-phase sequences indicates the presence of microscopic fat, whereas India ink artifact (a black line) is seen

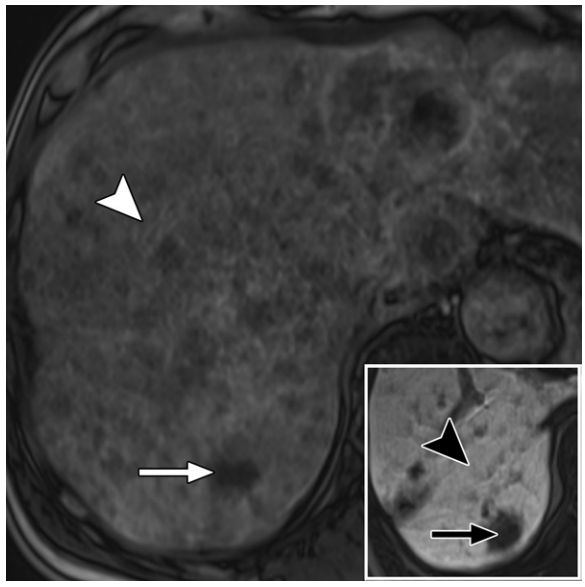

Figure 8. Axial MR images show the effects of liver dysfunction on background liver hyperintensity with gadoxetate-enhanced HBP imaging in a 69-year-old man with metastatic melanoma. In the setting of liver dysfunction and a serum total bilirubin level of 3.1 mg/dL, background liver signal intensity is diminished (white arrowhead) compared with normal liver signal intensity (black arrowhead) on an image from a prior examination (inset) when the bilirubin level was 1.2 mg/dL. A segment VII metastasis (black and white arrows) is depicted on both images, but with less contrast than the background liver with progressive liver dysfunction.

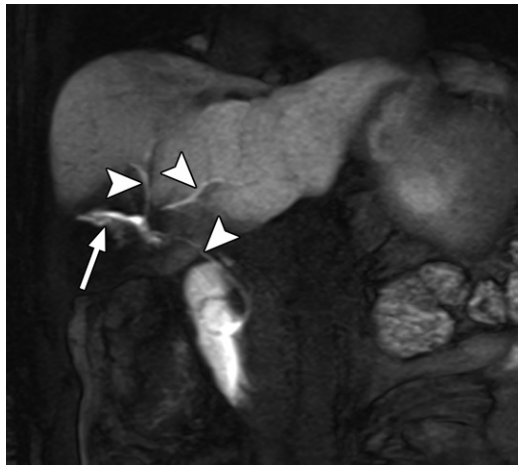

Figure 9. Gadoxetate bile leak imaging in a 28-year-old patient with a gunshot wound. Coronal T1-weighted HBP MR image obtained 60 minutes after the administration of gadoxetate shows leak of biliary contrast agent at the hepatic hilum (arrow) out of the normal biliary tree (arrowheads) from a gunshot injury.

at interfaces between macroscopic fat and water. The typical acquisition is a two-dimensional (2D) sequence performed over two to three breath holds with 5–8-mm sections. Advances in image processing algorithms and scanner technology have led to widespread availability of a 3D single breath-hold acquisition to produce typical

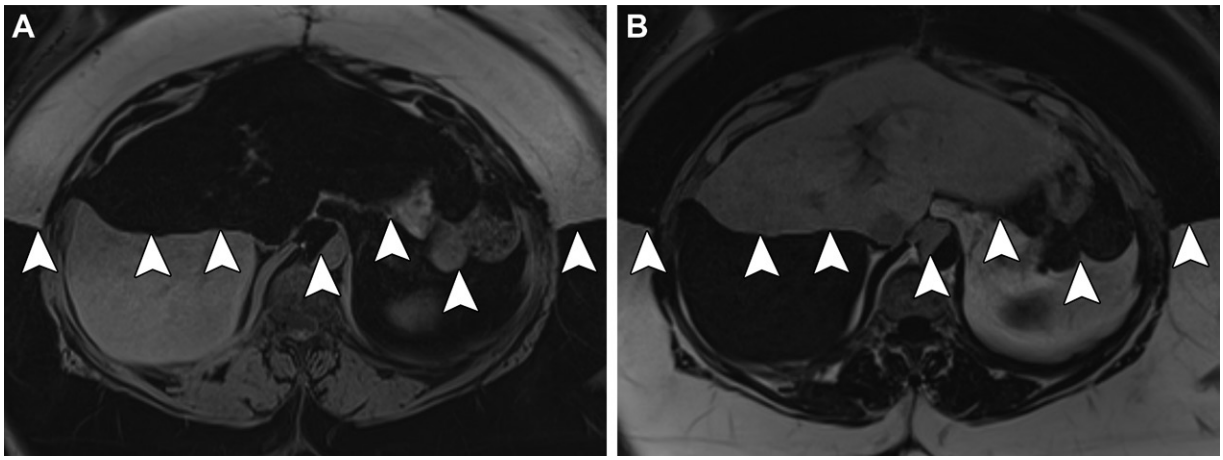

Figure 10. Dixon fat-water swap in a 60-year-old woman who underwent MRI of the abdomen and pelvis. Axial water-only Dixon MR image **(A)** shows unexpected fat-water swap anterior to a line demarcated by the arrowheads, where mathematical swap of where they should have been assigned has resulted in subcutaneous fat anteriorly being hyperintense and liver signal intensity similarly being misassigned. Axial fat-only Dixon MR image **(B)** shows corresponding fat-water swap, where subcutaneous fat anteriorly is hypointense and liver signal intensity anterior is incorrect.

in-phase and opposed-phase images with thinner sections (3–5 mm), which in our experience reading MRI examinations from outside institutions is infrequently used. These images can be leveraged to generate fat-only and water-only reconstructions via the Dixon method (21). Benefits of the 3D Dixon technique include better spatial resolution, shorter acquisition time, and additional diagnostically useful sequences, at the expense of potentially lower signal-to-noise ratio with thinner sections and fat-water swap artifacts. Both trade-offs are more common with older scanners, likely owing to less advanced parallel acceleration techniques and Dixon reconstruction algorithms (Fig 10). The utility of Dixon reconstructions will be detailed later in this article.

Problem Solving

Magnetic Susceptibility

Materials that alter the local magnetic field change the precessional frequency of adjacent tissue, leading to T2*-related signal loss, more pronounced with gradient-echo sequences with longer TEs. These materials include molecular oxygen in the air, iron from hemosiderin in blood products, and metallic devices. Images from the in-phase sequence (typically performed with longer TE) can be compared with those from the opposed-phase sequence (typically shorter TE) to identify sources of magnetic susceptibility, which are helpful to recognize in several clinical scenarios (22). Hemorrhage in a renal or hepatic cyst may manifest as a rim of magnetic susceptibility (Fig 11). Iron deposition in organs rapidly degrades MRI signal as TEs are increased. In patients with splenic siderosis, susceptibility can

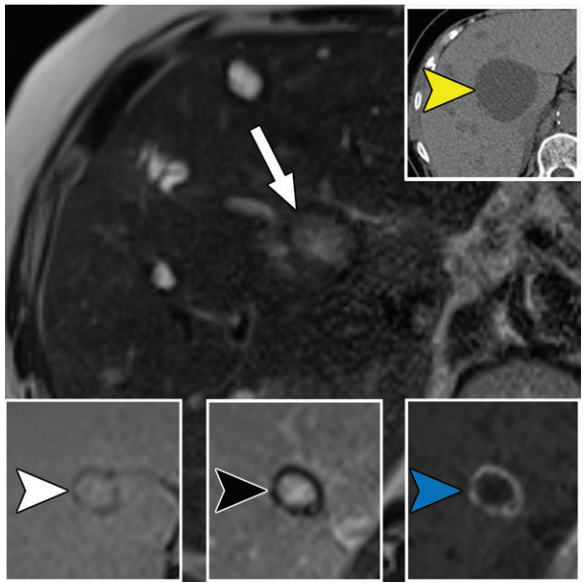

Figure 11. Magnetic susceptibility as a problem-solving tool in an 80-year-old woman with an involuted hemorrhagic hepatic cyst. Axial T2-weighted MR image shows an intermediate-T2-signal-intensity hepatic lesion with a thick hypointense rim (arrow). Gradient-echo images with a TE of 2.38 msec (bottom left inset) and 15.6 msec (bottom middle inset) show accentuation of hypointense signal with longer TE (white and black arrowheads) consistent with magnetic susceptibility from a hemosiderin rim from prior hemorrhage. An R2* map (bottom right inset) generated from multiecho gradient imaging shows corresponding hyperintensity (blue arrowhead), providing similar information with a single sequence compared with having to review sequential data from multiple echoes. Comparison with an axial CT image from 3 years prior (top right inset) shows a larger cyst in this location (yellow arrowhead) that hemorrhaged and involuted in the interim.

potentially help distinguish a splenule from a primary pancreatic mass (Fig 12). Free air, which is straightforward to diagnose at CT, can be more challenging to identify at MRI. A potential tool is an R2* map, which can be generated from multi-

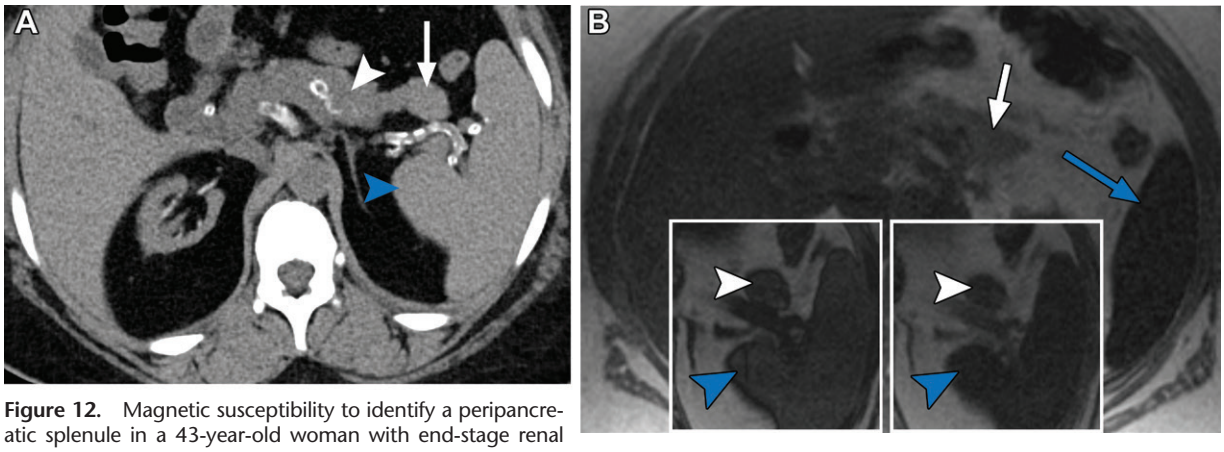

Figure 12. Magnetic susceptibility to identify a peripancreatic splenule in a 43-year-old woman with end-stage renal disease. **(A)** Axial nonenhanced CT image shows a slightly lobulated mass (arrow) between the pancreas (white arrowhead) and spleen (blue arrowhead). **(B)** Axial in-phase MR image shows hypointensity of the spleen (blue arrow) relative to the pancreas (white arrow), indicative of splenic iron deposition. The peripancreatic mass (white arrowheads) follows the signal intensity of the spleen (blue arrowheads) when comparing the shorter-TE opposed-phase (left inset) and longer-TE in-phase (right inset) images, consistent with a peripancreatic splenule.

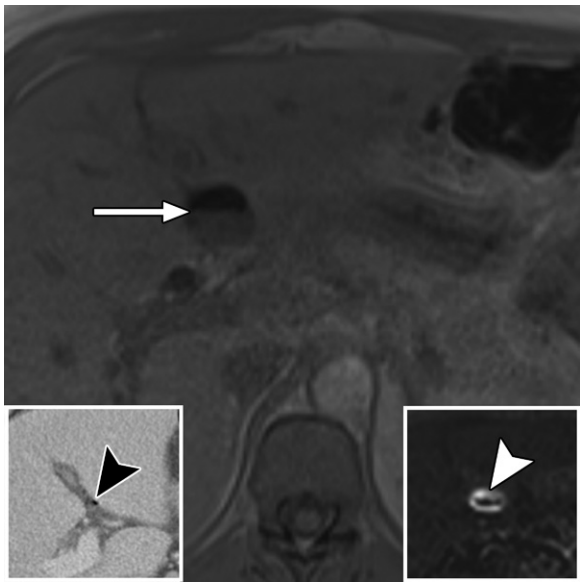

Figure 13. Pneumoperitoneum identified at MRI as magnetic susceptibility artifact in a 39-year-old woman with a perforated duodenal ulcer. A tiny locule of free air in the porta hepatis (black arrowhead) was not identified on the axial CT image (left inset). Subsequent axial in-phase MR image obtained a few days later shows an air-fluid level (arrow) in the porta hepatis, with corresponding hyperintense signal (white arrowhead) on the R2* map (right inset) generated from multiecho gradient imaging consistent with pneumoperitoneum. Exploratory laparotomy confirmed a perforated duodenal ulcer.

echo gradient imaging (eg, Siemens LiverLab, GE StarMap) on newer platforms. R2* is the reciprocal of T2*, and higher signal intensity on the R2* map corresponds to greater magnetic susceptibility within a voxel. This approach can make foci of susceptibility, such as free air, more noticeable (Fig 13) (23).

Magnetic susceptibility may also lead to misdiagnosis, as blooming artifact from surgical clips can mimic disease. HBP hypointense foci along the surface of the liver should be carefully assessed at in-phase and opposed-phase imaging to exclude susceptibility from surgical clips as the cause of the finding. DWI may also be helpful owing to sensitivity of the echo-planar imaging technique to magnetic susceptibility also highlighting the blooming artifact (Fig 14).

Subtraction Imaging

Dynamic imaging without additional ionizing radiation is a core advantage of body MRI compared with CT. Furthermore, MRI affords the opportunity to subtract the signal intensity of precontrast images from postcontrast images on a voxel-by-voxel basis, making enhancement more conspicuous (24). This is particularly helpful when a finding is intrinsically T1 hyperintense, making enhancement difficult to assess (eg, hemorrhagic lesions, nodules in the cirrhotic liver, posttreatment imaging after ablation or locoregional therapy). Some picture archiving and communication system (PACS) vendors offer the ability to generate subtraction images as needed, and technologists can usually generate these after examination completion, if requested by the radiologist. However, to streamline our workflow, we routinely generate subtraction images as part of the standard protocol at all body MRI examinations.

Misregistration and vascular inflow artifacts are two important pitfalls with subtraction imaging. Misregistration, where the finding of interest has "moved" between precontrast and postcontrast sequences owing to differing breath holds, can lead to misdiagnosis of enhancement or nonenhancement (Fig 15). Findings should always be confirmed on the source images. Vascular inflow artifacts at the edge of the imaging volume may result

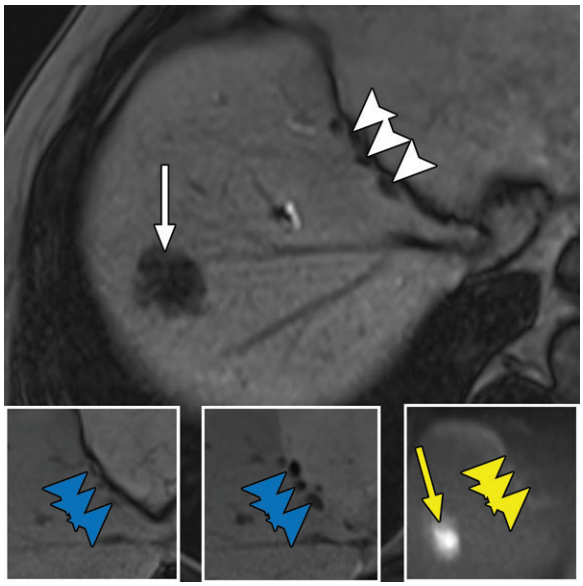

Figure 14. Susceptibility artifacts from surgical clips mimicking subcapsular hepatic metastases in a 62-year-old-man with metastatic colon cancer after left hemihepatectomy. Axial T1-weighted HBP MR image shows a segment VII hypointense hepatic metastasis (white arrow) and several hypointense foci along the surface of the right hemiliver (white arrowheads), which might be mistaken for metastases along the resection margin. However, there is no corresponding diffusion restriction (right inset, yellow arrowheads), unlike the hyperintense metastasis (yellow arrow). Blooming artifact (blue arrowheads) is depicted with accentuation of hypointensity on the longer-TE in-phase image (middle inset) compared with on the shorter-TE opposed-phase image (left inset), confirming susceptibility artifact from clips as the source of these imaging findings.

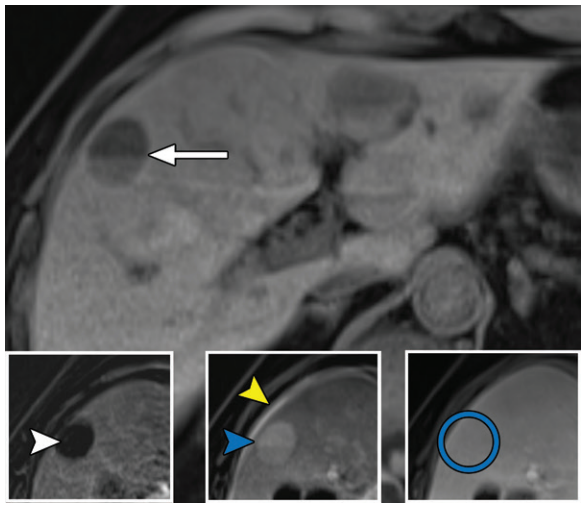

Figure 15. Subtraction misregistration artifact in a 79-year-old man with metastatic angiosarcoma. Axial precontrast T1-weighted MR image shows a fluid-fluid level within a hypointense liver lesion (arrow). Subtracted T1-weighted arterial phase MR image (left inset) shows no lesion enhancement (white arrowhead). Subtracted T1-weighted delayed phase MR image (middle inset) shows apparent enhancement (blue arrowhead), but when correlated with the source delayed phase image (right inset), this "enhancement" is due to through-plane misregistration from the patient taking a slightly different breath hold, resulting in normal parenchyma (blue circle) being subtracted by the lesion. In-plane misregistration is also evident with a hyperintense rim (yellow arrowhead) around the liver (middle inset) that is not present on the source image (bottom right inset).

in luminal hyperintensity on precontrast images, producing a signal void and mimicking thrombosis at postcontrast subtraction imaging (Fig 16).

Transient Hepatic Intensity Difference

Transient hepatic intensity difference (THID), in which a portion of the liver hyperenhances during the arterial phase but equilibrates with background liver in later phases, is a vascular phenomenon due to alterations in relative blood supply from the hepatic artery versus the portal vein. Identification of THID should prompt the reader to search for processes such as portal vein thrombosis, biliary obstruction, or narrowing of the portal vein or hepatic artery (Fig 17) (25). Infectious and inflammatory conditions such as hepatic abscesses and cholangitis may also lead to THID (Fig 18). As alterations in hepatic enhancement may obscure masses, review of T1-weighted precontrast images can be helpful to improve conspicuity. When no underlying cause is identified, THID can be deemed idiopathic.

Parallel Imaging

Parallel imaging increases acquisition speed by using a multicoil array, partial k-space sampling, and computational data "unwrapping" based on coil sensitivities. Undersampling of k-space in the phase-encoding direction results in aliasing, which may not be fully eliminated in the unwrapping process (26). Persistent aliasing can mimic aortic dissection by "duplication" of the abdominal wall contour (Fig 19) or obscure findings in the liver. More advanced parallel imaging techniques (eg, axial controlled aliasing in parallel imaging results in higher acceleration [CAIPIRINHA]; Siemens) ameliorate this problem.

Fat

Steatosis

Diffuse hepatic steatosis is commonly diagnosed by observing diffuse signal loss on opposed-phase images compared with in-phase images. Less commonly, steatosis may be nodular, focal, and infiltrative, requiring careful attention to chemical shift imaging (27). Focal fat occurs in characteristic locations, such as adjacent to the falciform ligament, gallbladder fossa, and porta hepatis. This may be intermittently apparent at serial CT examinations owing to differences in contrast timing. T1-weighted postcontrast and HBP imaging (both performed with opposed-phase TEs) will show hypointensity to background liver,

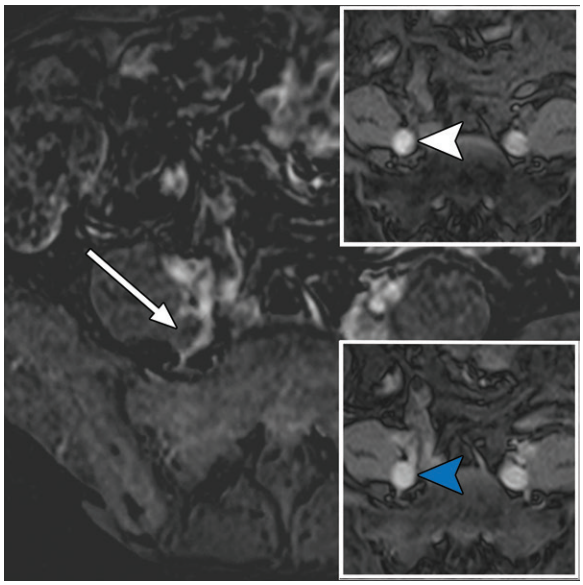

Figure 16. Subtraction inflow artifact in a 50-year-old woman with breast cancer who underwent liver MRI. Axial subtracted T1-weighted delayed phase MR image shows an apparent filling defect in the right common iliac vein (arrow). However, comparison with the precontrast T1-weighted MR image (top inset) shows hyperintense signal (white arrowhead) owing to vascular inflow of unsaturated protons, resulting in artifactual hypointensity (blue arrowhead) when subtracted from the source T1-weighted delayed phase MR image (bottom inset). Vascular inflow artifact is common at the top and bottom of an axial 3D volume.

potentially mimicking metastasis. Focal lesions in the characteristic locations mentioned previously should prompt additional scrutiny with chemical shift sequences and fat-only Dixon imaging to diagnose focal fat (Fig 20). Steatosis may also be nodular, mimicking diffuse malignancy (Fig E5), or infiltrative and/or masslike in appearance (Fig 21). Fat-only Dixon imaging is particularly helpful when there are distracting findings with opposed-phase imaging, as every voxel without fat will be hypointense, improving fat conspicuity (Fig 21). When considering an unusual pattern of steatosis, reviewing diffusion-weighted images is helpful as steatosis does not typically result in hyperintensity at high *b*-value DWI.

A pitfall to avoid in severely steatotic livers is misinterpreting a focal "T1 hyperintensity" on an opposed-phase image. To reduce acquisition time, fat-suppressed T1-weighted 3D sequences are routinely performed with the minimum TE (in the opposed phase), causing diffuse background signal loss in a steatotic liver. The in-phase sequence is thus more accurate for determining if a lesion is truly T1 hyperintense and potentially hemorrhagic (Fig E6) (28), rather than a visual interpretive error because of how the adjacent liver signal intensity changes owing to chemical shift.

Steatosis may also occur in the pancreas in the form of diffuse or geographic fatty deposition or

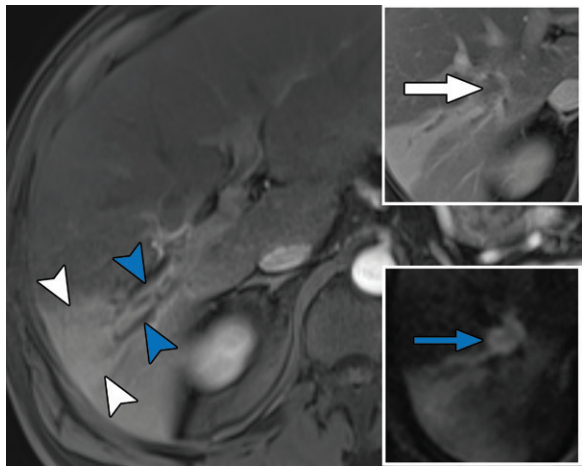

Figure 17. THID from a hepatic metastasis in a 39-year-old man with metastatic colorectal cancer. Axial T1-weighted arterial phase MR image shows THID (white arrowheads) in the right posterior section and peripheral biliary ductal dilatation (blue arrowheads). T1-weighted portal venous phase MR image (top inset) shows a central hypoenhancing liver metastasis (white arrow) as the cause of biliary obstruction and resultant THID. Diffusion-weighted image (bottom inset) helps identify the metastasis (blue arrow), which may otherwise be obscured by adjacent THID.

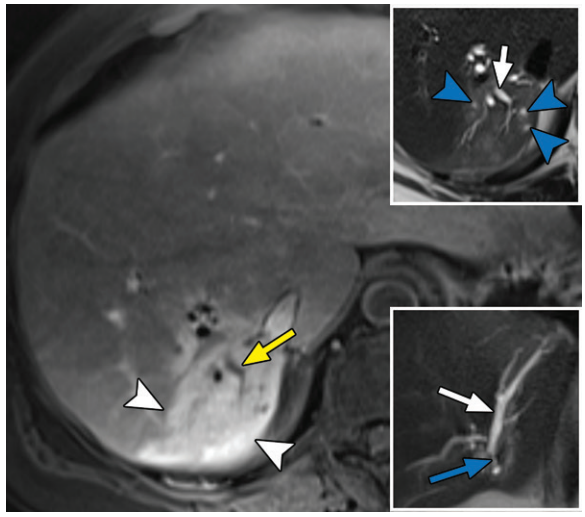

Figure 18. THID from biliary abscesses and obstruction in a 57-year-old woman after Roux-en-Y hepaticojejunostomy after bile duct injury. Axial T1-weighed arterial phase MR image shows THID in hepatic segment VII (white arrowheads) with dilated peripheral bile ducts (yellow arrow). Axial (top inset) and coronal (bottom inset) T2-weighted MR images show biliary ductal dilatation (white arrows) owing to a hepaticojejunal anastomotic stricture (blue arrow) causing biliary microabscesses (blue arrowheads) as the source of THID.

focal fat lobules (29,30). Tiny fat lobules mimic a branch duct intraductal papillary mucinous neoplasm (IPMN) at CT, T2-weighted MRI, and postcontrast T1-weighted MRI, potentially leading to unnecessary follow-up. If no corresponding abnormality is seen on fat-suppressed heavily T2-weighted images, chemical shift sequences should be scrutinized for India ink artifact or

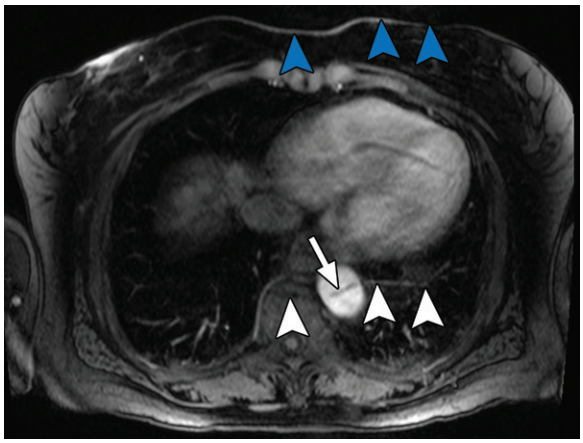

Figure 19. Parallel imaging wrap artifact mimicking aortic dissection in a 63-year-old woman who underwent liver MRI. Axial T1-weighted arterial phase MR image shows an apparent "dissection flap" in the descending thoracic aorta (arrow). However, the line extends outside of the aorta, overlying the spine and left lung (white arrowheads), and recapitulates the anterior abdominal wall (blue arrowheads), consistent with an "unwrapping" artifact from parallel imaging reconstruction on an older MRI scanner.

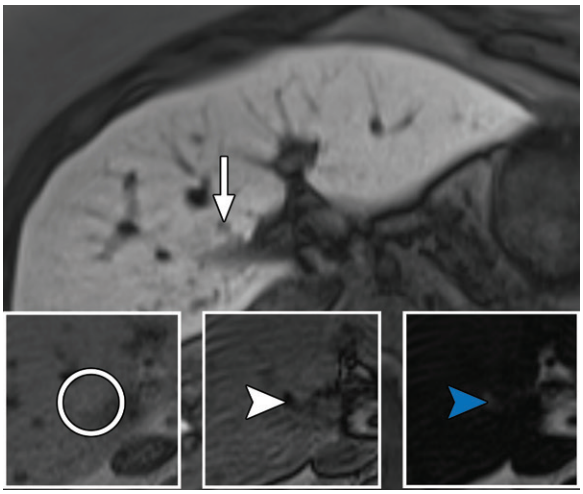

Figure 20. Focal hepatic steatosis mimicking hepatic metastasis in a 63-year-old woman with metastatic leiomyosarcoma. Axial T1-weighted HBP MR image shows a hypointense lesion (arrow) corresponding to the finding at CT that prompted MRI. In-phase (left inset) and opposed-phase (middle inset) chemical shift MR images show focal hypointensity (white arrowhead) at opposed-phase imaging compared with that at in-phase imaging (circle), consistent with focal fat. Fat-only Dixon image (right inset) shows corresponding hyperintensity (blue arrowhead). Dixon imaging is a useful additional technique for depicting steatosis.

hyperintensity on fat-only Dixon images to confirm intrapancreatic fat (Fig E7).

Failure of Fat Suppression

Frequency-selective fat saturation, in which a radiofrequency pulse selectively excites fat protons for signal spoiling, is one of the most commonly used fat-suppression methods in body MRI (31). However, this method presupposes a dominant fat

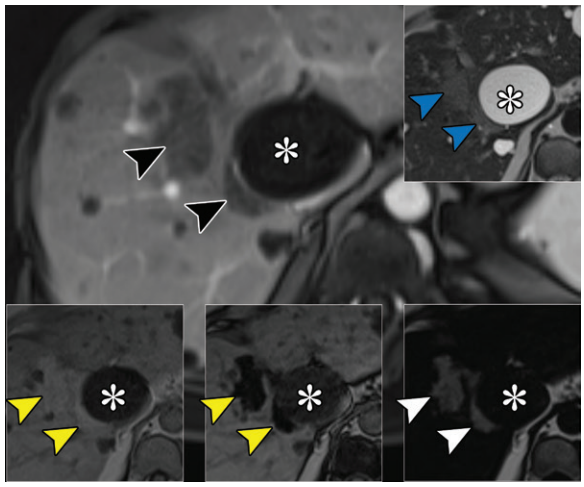

Figure 21. Masslike steatosis mimicking infiltrative malignancy in a 65-year-old woman with necrotizing pancreatitis. Axial T1-weighted portal venous phase MR image shows hypoattenuating "masses" (black arrowheads) with corresponding intermediate hyperintensity at T2-weighted imaging (top right inset, blue arrowheads), which might raise suspicion for malignancy. Opposed-phase chemical shift MR image (middle inset) shows marked hypointensity of these foci (yellow arrowheads) compared with on the in-phase image (left inset), consistent with steatosis. The fat-only Dixon image (right bottom inset) shows focal steatosis with maximal contrast (white arrowheads), as the remainder of the liver, including an adjacent cyst (*), has no signal.

signal intensity peak that the scanner can readily identify. In our experience, this automated process may fail at 3 T in patients with obesity (Fig 22). The technologist can potentially overcome this by repeating the sequence after selecting the portion of the field of view to interrogate for manual selection of the dominant fat peak. Alternate fat-suppression methods can also be used, such as STIR (for T2-weighted precontrast imaging), spectral adiabatic inversion recovery (SPAIR), or the Dixon method. The Dixon method is more robust to B_0 (main static magnetic field) and B_1 (rotating magnetic field) inhomogeneity and can be used after contrast agent administration. However, it results in longer minimum repetition time (TR) owing to the dual-echo acquisition, increasing imaging time unless fewer or thicker sections are obtained (32). Fat-water swap may also occur and necessitate reconstruction of fat-only sequences. In our practice, we currently use frequency-selective fat suppression for dynamic imaging and use the Dixon method only on protocols (eg, 3-T prostate MRI) for which fat suppression may be challenging.

Bone Evaluation

Spin-echo T1-weighted imaging is less frequently used in body MRI, with limited utility for assessing the abdominopelvic viscera. Chemical shift imaging provides a valuable alternative to identify marrow-replacing lesions at body MRI, particularly if the Dixon method is used

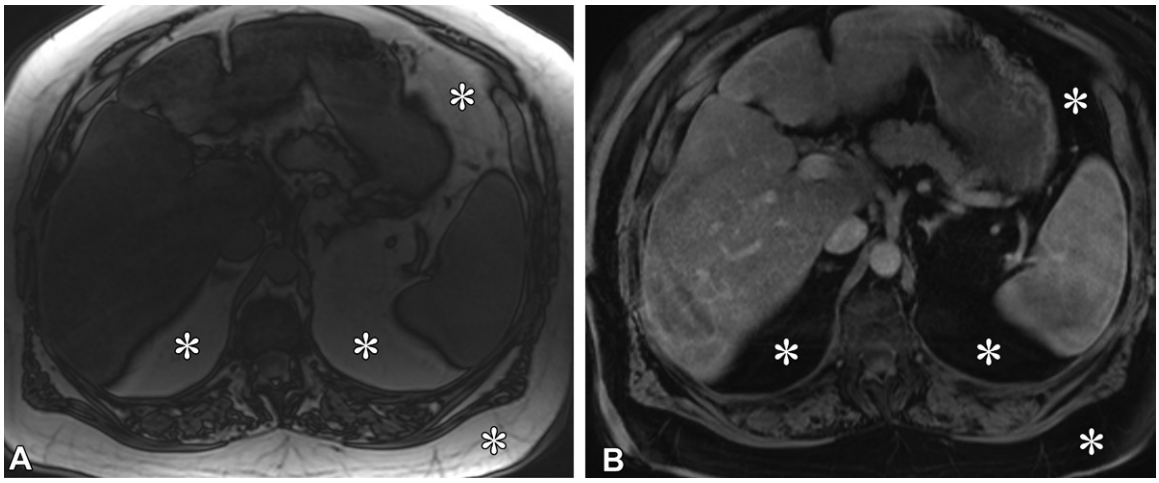

Figure 22. Failure of frequency-selective fat saturation in a 59-year-old-man with HCC. **(A)** Axial precontrast T1-weighted MR image shows global failure of fat suppression (*). The image is similar in appearance to that seen with an opposed-phase sequence owing to this sequence typically being performed with the shortest possible TE. **(B)** Axial T1-weighted delayed phase water-only Dixon MR image shows successful fat suppression (*), which can be used before and after contrast agent administration..

(33). Fat-only Dixon imaging can be used as a screening tool to identify potentially suspicious bone findings that can then be assessed in more detail with other sequences (Fig 23). Notably, a focal hypointense lesion does not equate to malignancy, as benign entities such as atypical hemangiomas, Schmorl nodes, and bone islands may also have this appearance (34,35).

Fat-containing Renal Masses

Fat in a renal mass limits the differential diagnosis and should be carefully sought (Fig 24) (36). Macroscopic fat is identifiable as signal loss after application of fat-suppression techniques, as India ink artifact on opposed-phase images at the fat-water interface or as signal intensity matching that of adjacent retroperitoneal fat on fat-only Dixon images. In contrast, microscopic fat exhibits signal loss on opposed-phase images or can be identified as signal intensity on fat-only Dixon images less than that of retroperitoneal fat. Macroscopic fat usually indicates a fat-rich angiomyolipoma (AML). Rare cases of clear-cell renal cell carcinoma with osseous metaplasia (37) and entrapment of renal sinus fat by oncocytomas have been described (38).

The identification of microscopic fat should prompt inspection of T2-weighted images. Most T2-hyperintense (on non-fat-suppressed images) microscopic fat-containing masses will represent clear-cell renal cell carcinoma, particularly if there is avid corticomedullary phase hyperenhancement (Fig 25) (39). T2 hypointensity in a microscopic fat-containing mass suggests fat-poor AML (in conjunction with additional features such as an arterial-to-delayed enhancement ratio >1.5) and should prompt consideration of biopsy if surgical resection is being considered to avoid unnecessary interventions (Fig 26) (40). As some clear-cell renal cell carcinomas will atypically be T2 hypointense, fat-poor AMLs should not be definitively diagnosed at imaging alone.

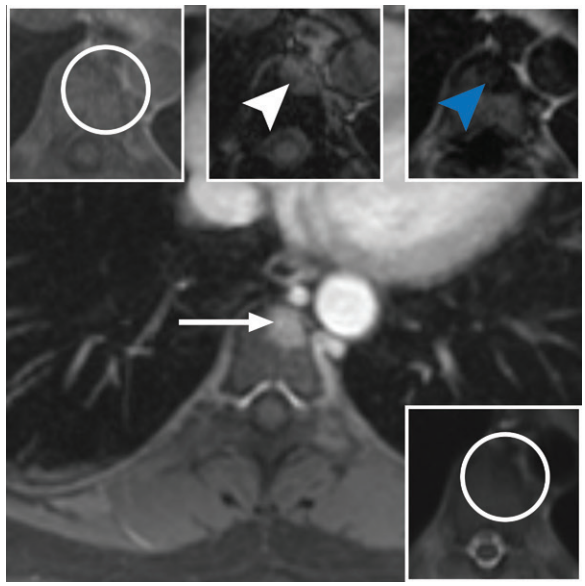

Figure 23. Fat-only Dixon imaging for evaluation of bone metastases at body MRI in a 49-year-old woman with breast cancer. Axial T1-weighted delayed phase MR image shows an enhancing thoracic spine lesion (arrow), without correlate (circles) on T2-weighted (bottom right inset) and precontrast in-phase (top left inset) MR images. Precontrast opposed-phase MR image (top middle inset) shows a lack of chemical shift signal loss in the lesion (white arrowhead), with corresponding hypointensity (blue arrowhead) on the fat-only Dixon image (top right inset), suggestive of the absence of microscopic fat. Metastasis was suggested and subsequently confirmed by the results of a bone biopsy.

Fat-containing Adrenal Masses

Like renal masses, fat in an adrenal mass similarly limits the differential diagnosis (Fig 27) (36).

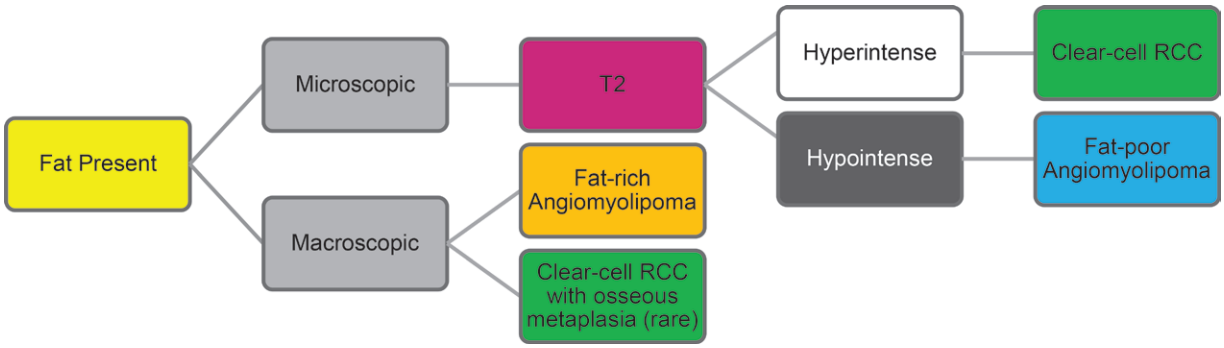

Figure 24. Fat-containing renal mass diagnostic algorithm. Microscopic fat should be distinguished from macroscopic fat by using chemical shift, Dixon, and fat-suppression techniques. If macroscopic fat is present, a fat-rich angiomyolipoma (AML) is almost always the diagnosis. If microscopic fat is present, T2 signal intensity should next be assessed. T2-hyperintense microscopic fat-containing masses are typically clear-cell renal cell carcinoma (RCC), with avid corticomedullary phase hyperenhancement. T2 hypointensity within a microscopic fat-containing renal mass should raise the possibility of a fat-poor AML, although imaging is not completely diagnostic.

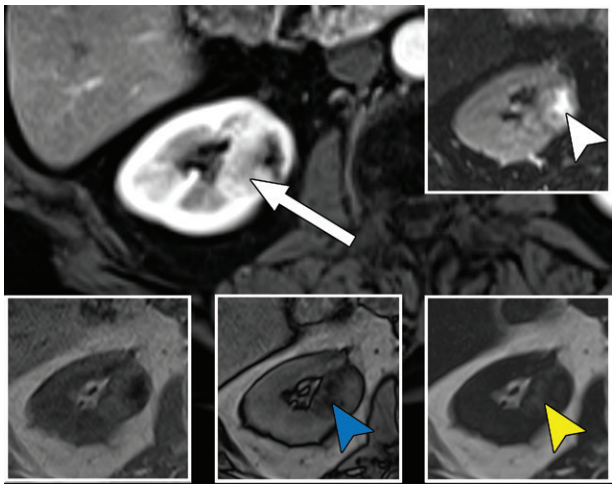

Figure 25. Clear-cell renal cell carcinoma with microscopic fat in a 65-year-old man. Axial T1-weighted arterial phase MR image shows an avidly enhancing right renal mass (arrow). Microscopic fat is identified with chemical shift signal loss (blue arrowhead) between the in-phase (bottom left inset) and opposed-phase (bottom middle inset) sequences and hyperintensity (yellow arrowhead) on the fat-only Dixon image (bottom right inset). Fat-suppressed T2-weighted MR image (top inset) shows hyperintensity (white arrowhead) within the lesion. A clear-cell renal cell carcinoma was confirmed at partial nephrectomy.

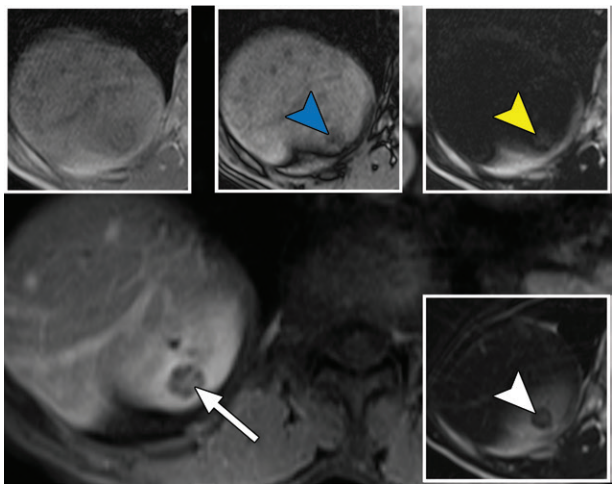

Figure 26. AML with microscopic fat in an 84-year-old man. Axial T1-weighted arterial phase MR image shows a hypoenhancing right upper renal mass (arrow). Microscopic fat is identified with chemical shift signal loss (blue arrowhead) between the in-phase (top left inset) and opposed-phase (top middle inset) sequences and hyperintensity (yellow arrowhead) on the fat-only Dixon image (top right inset). T2-weighted MR image (bottom inset) shows hypointensity (white arrowhead) within the lesion, suggesting a fat-poor renal AML.

Macroscopic fat is essentially diagnostic of adrenal myelolipoma, with rare exceptions including liposarcoma or AML. If macroscopic fat is not easily identifiable, India ink artifact on opposed-phase images should be sought (Fig 28).

Microscopic fat-containing adrenal masses are most commonly fat-rich adenomas, but T2 hyperintensity, size, and clinical history should also be considered. Most adenomas are isointense to slightly hyperintense to liver with T2-weighted sequences (if the liver is not steatotic or siderotic) (41). T2 hyperintensity relative to liver warrants further investigation, with marked T2 hyperintensity raising suspicion for a pheochromocytoma. Large size, necrosis, and hemorrhage often indicate adrenocortical carcinoma, which rarely contains microscopic fat (42). Microscopic fat-containing metastases to the adrenal gland should be considered in the setting of prior steatotic primary malignancies, such as clear-cell renal cell carcinoma or HCC (Fig 29). Metastatic disease may also form collision tumors with preexisting fat-rich adenomas (43).

Motion

Motion artifact attributable to respiratory motion is the most common cause of a nondiagnostic or suboptimal body MRI examination. These artifacts can be mitigated by increasing acquisition speed to shorten breath holds, using motion-insensitive acquisition techniques, or utilizing respiratory triggering (44).

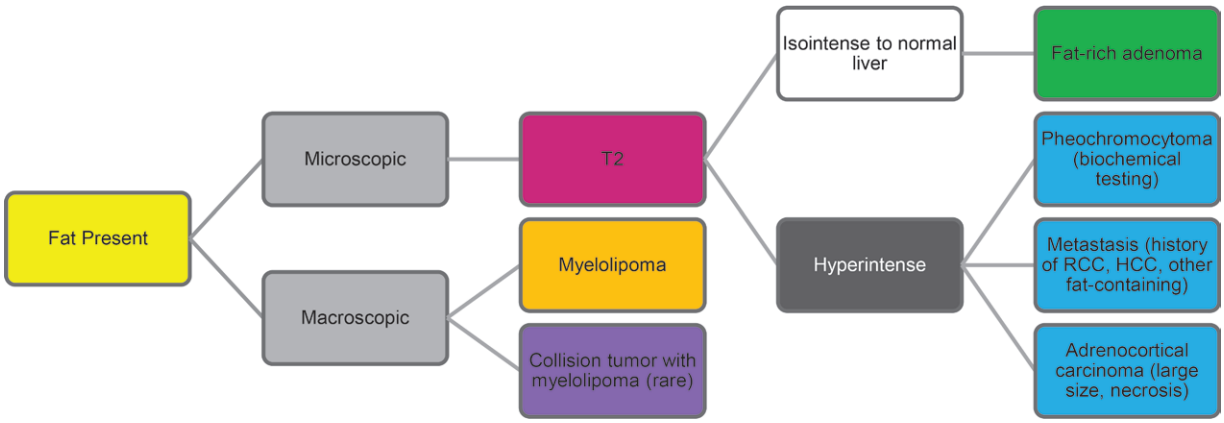

Figure 27. Fat-containing adrenal mass diagnostic algorithm. Microscopic fat should be distinguished from macroscopic fat by using chemical shift, Dixon, and fat-suppression techniques. If macroscopic fat is present, an adrenal myelolipoma is almost always the diagnosis. If microscopic fat is present, T2 signal intensity should next be assessed. T2-isointense microscopic fat-containing masses are almost always fat-rich adenomas. If T2 hyperintensity greater than that of the normal liver is present, other masses should be considered based on patient history, symptoms, lesion size, and other imaging features such as the degree of T2 hyperintensity and presence of necrosis or vascular invasion. *RCC* = renal cell carcinoma.

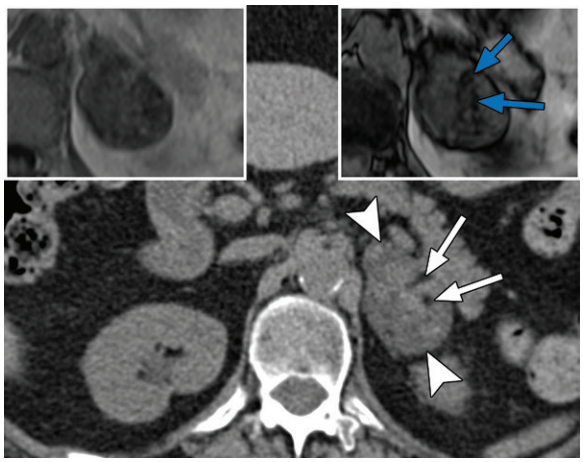

Figure 28. Adrenal myelolipoma incidentally identified at lung-screening chest CT in a 69-year-old woman. Axial nonenhanced CT image shows foci of macroscopic fat (white arrows) within a large left adrenal mass (arrowheads), consistent with adrenal myelolipoma. Subsequent axial MR images show internal India ink artifact (blue arrows) when comparing the opposed-phase MR image (right inset) to the in-phase image (left inset), a helpful clue when only small amounts of microscopic fat are present.

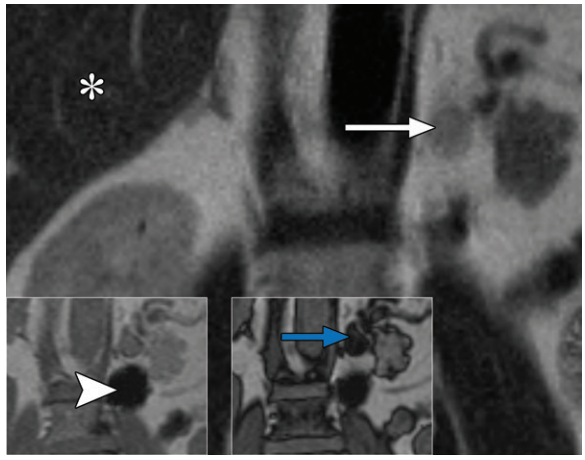

Figure 29. Microscopic fat-containing adrenal mass in a 64-year-old man after nephrectomy. Coronal T2-weighted MR image shows a left adrenal mass (white arrow), which is T2 hyperintense relative to normal liver (*). In-phase (left inset) and opposed-phase (right inset) MR images show chemical shift signal loss (blue arrow) on the opposed-phase image consistent with microscopic fat. An adrenal mass that is T2 hyperintense relative to liver should prompt further consideration beyond adenoma. The patient had undergone nephrectomy, and blooming artifact from surgical clips (arrowhead) is evident on the longer-TE in-phase image (left inset). In this case, renal cell carcinoma was confirmed by the results of a biopsy. In a patient with clear-cell renal cell carcinoma, metastasis must be considered when a lesion contains microscopic fat.

Parallel imaging, as described previously, is routinely used with T1-weighted sequences to increase acquisition speed, typically with an acceleration factor (R) of 2 or more. Higher Rs can be achieved via two-dimensional phase-shifted data sampling to achieve more rapid imaging with fewer artifacts. This approach uses coil sensitivities across an entire volume of imaged tissue, allowing fourfold ($R = 2 \times 2 = 4$) or higher Rs (Fig E8). This can also be further leveraged in coronal acquisitions, given the greater number of coil elements in the craniocaudal direction for a typical multichannel phased-array coil, to achieve breath-hold acquisitions in as few as 5 seconds.

Compressed sensing is another acceleration technique based on semi-random undersampling of k-space. Dynamic T1-weighted imaging utilizing compressed sensing (as discussed previously) is ideal for patients with difficulty breath holding and is typically performed during free breathing (45). Compared with breath-hold images in the same patient, compressed sensing reduces motion artifact, improving diagnostic yield (Fig E9). Compressed sensing can also be applied to 3D

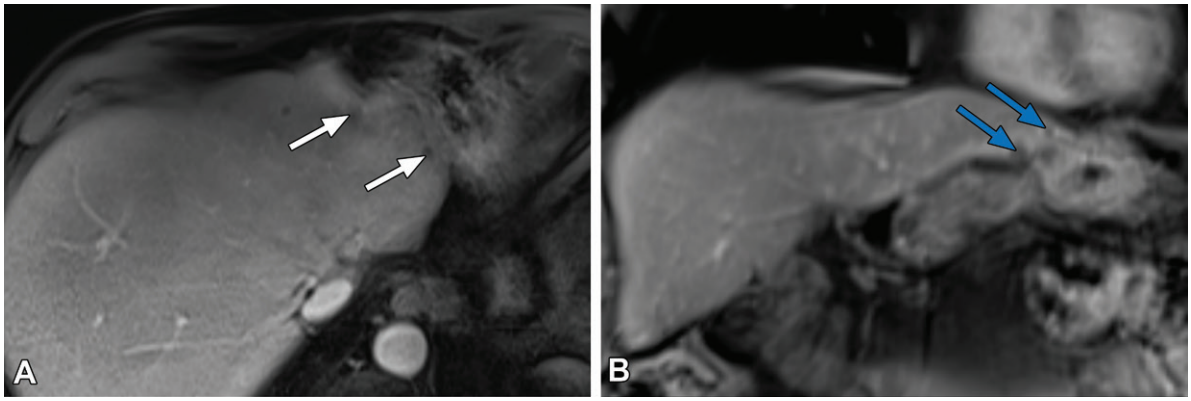

Figure 30. Subtle left lateral section hepatic lesions in a 71-year-old man with HCC after radioembolization. **(A)** Axial T1-weighted MR image shows that evaluation of the margin of the left lateral section of the liver is often challenging at axial T1-weighted MRI owing to volume averaging with the stomach and cardiac pulsation artifacts. Two small lesions are present (arrows) but were not initially identified. **(B)** Coronal T1-weighted delayed phase MR image shows the lesions to better advantage (arrows), prompting reassessment at axial imaging.

MR cholangiopancreatography, reducing acquisition times two-to-threefold for a free-breathing technique or to a single breath hold by using even greater Rs (Fig E10) (46).

Radial k-space sampling is a motion-insensitive technique applicable to either T1- or T2-weighted sequences. It is generally performed during free-breathing, with longer acquisition times than conventional sequences. In contrast to Cartesian k-space filling, two-dimensional radial trajectories (eg, BLADE [Siemens], Propeller [periodically rotated overlapping parallel lines with enhanced reconstruction; GE]) fill k-space by using a rotating acquisition in which the center of k-space is sampled during each readout, allowing motion correction, rejection of data degraded by motion, and dispersion of in-plane motion artifacts (47). The periphery of k-space is relatively undersampled and the center is oversampled; consequently, edge blurring and radial streak artifacts are common. Radial k-space acquisitions can also be applied to 3D T1-weighted sequences by using a stack-of-stars trajectory (eg, StarVIBE [Siemens]; MultiVane XD [Philips]) in which rotating spokes are acquired in plane with a Cartesian trajectory through the plane, facilitating a free-breathing sequence with reduced motion (48). The longer acquisition time (~3 minutes) makes this technique suitable for nondynamic imaging (eg, HBP or delayed phase) (Fig E11).

Finally, respiratory triggering links image acquisition to the respiratory cycle by using either a navigator pulse to track diaphragmatic position or a physical respiratory bellows device to trigger acquisitions from body wall excursions (49). Free-breathing acquisitions, such as 3D MR cholangiopancreatography, are typically obtained with respiratory navigation, and T2-weighted sequences such as single-shot and fat-suppressed turbo spin echo (TSE) may also be performed with respiratory navigation. DWI is performed more rapidly with a free-breathing nonnavigated technique, but motion artifacts can be reduced with respiratory navigation at the expense of longer acquisitions (50).

Challenging Anatomic Sites

The mesentery and omentum can be difficult to assess at abdominal MRI owing to bowel motion artifact, failure of fat suppression at the periphery, and limited field of view inferiorly. Coronal T2-weighted and postcontrast T1-weighted sequences often provide the largest field of view for assessment of these structures, with no additional acquisition time penalty in the frequency-encoding direction (Fig E12). DWI helps detect abnormalities, prompting further assessment with other sequences (51).

Similarly, thoracic findings, such as breast or mediastinal masses, are also easy to miss at abdominal MRI. DWI is quite sensitive for body wall abnormalities, although artifacts on older scanners may limit evaluation because of B_0 inhomogeneity (Fig E13). Coronal T2-weighted imaging is invaluable in identifying unsuspected abnormalities, and we routinely perform pre- and postcontrast coronal T1-weighted sequences (including subtractions) to improve detection and characterization of incidental thoracic findings (Fig E14).

Specific regions of the hepatobiliary system are inherently difficult to evaluate at body MRI. The left lateral section of the liver is often obscured by cardiac pulsation artifact and volume averaging with the stomach. Coronal imaging is particularly valuable in assessing this location (Fig 30). Subcapsular liver lesions can also be troublesome on HBP images, as hypointense lesions can be masked by adjacent fat or lung.

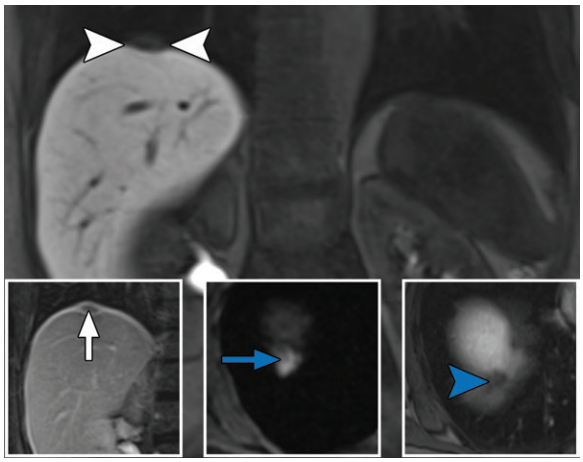

Figure 31. Subtle subcapsular hepatic metastasis in a 55-year-old woman with metastatic ovarian cancer. Coronal T1-weighted HBP MR image after Eovist administration does not conspicuously show a metastasis along the dome of the liver (white arrowheads) owing to poor contrast between HBP hypointensity and adjacent lung. The lesion is also poorly noticeable on the axial T1-weighted HBP MR image (right inset, blue arrowhead) but can be seen to greater advantage on the coronal T1-weighted delayed phase MR image (left inset, white arrow) and diffusion-weighted image (middle inset, blue arrow). While HBP imaging often provides the greatest contrast for detecting hepatic metastases, the edges of the liver should be carefully inspected with other sequences to avoid overlooking such lesions.

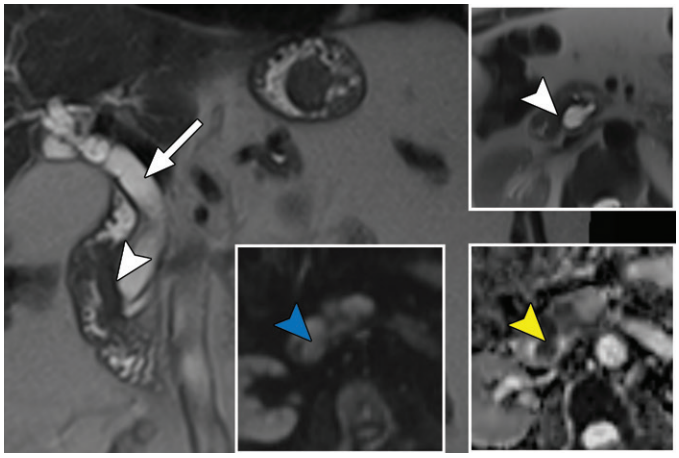

Figure 32. Overlooked ampullary mass in a 69-year-old woman with jaundice. Coronal T2-weighted MR image shows biliary ductal dilatation (arrow). The ampullary mass (white arrowheads) was not identified prospectively, with similar signal intensity to the normal duodenal wall on the coronal and axial (top right inset) T2-weighted MR images. Diffusion-weighted image (bottom left inset) and ADC map (bottom right inset) show diffusion restriction (blue arrowhead) and ADC hypointensity (yellow arrowhead), valuable clues for diagnosis that were identified at imaging review before endoscopic biopsy, the results of which confirmed ampullary adenocarcinoma.

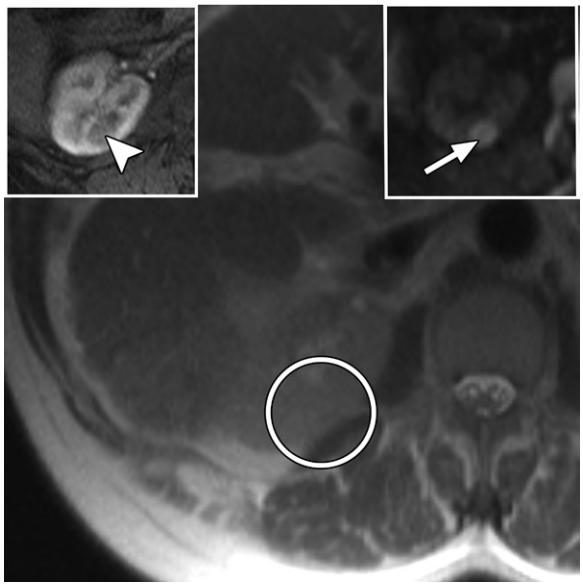

Figure 33. Greater conspicuity of a renal mass with DWI in an 82-year-old woman who underwent liver MRI for cirrhosis. Axial T2-weighted MR image does not show any renal cortical abnormality (circle). Diffusion-weighted image (right inset) shows a rounded hyperintensity (arrow) corresponding to a hypoenhancing mass (arrowhead) on the T1-weighted arterial phase MR image (left inset), which may be easily overlooked with other sequences but is highly conspicuous with DWI.

The HBP is often best assessed in both axial and coronal planes, in conjunction with portal venous phase T1-weighted sequences and DWI to avoid overlooking potential disease sites (Fig 31). The periampullary region can present difficulty in detecting masses with T2-weighted sequences owing to their similar signal intensity to that of the pancreas or duodenal wall. DWI and multiplanar thin-section T2-weighted sequences are particularly useful in this regard (Fig 32).

Tips for Interpretation

Diffusion-weighted Imaging

DWI often provides the greatest lesion conspicuity of any noncontrast sequence in a body MRI protocol. However, diffusion restriction should not be equated with malignancy, as both benign and malignant entities can restrict diffusion (52). Causes of diffusion restriction include normal and abnormal lymphoid tissue, tumors, blood products, inflammation, and purulent material (51,53). The superb contrast of DWI helps identify lesions that may blend with normal parenchyma with T1- or T2-weighted sequences, such as subtle renal masses (Fig 33). Assessment

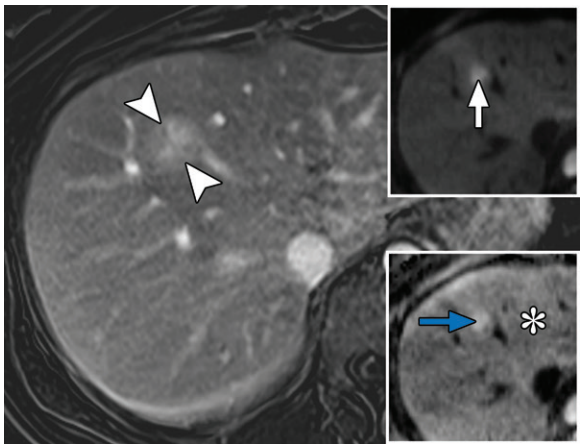

Figure 34. Interpretation of T2 shine-through at DWI in a 27-year-old woman with Li-Fraumeni syndrome who underwent MRI to evaluate a liver lesion depicted at whole-body screening MRI. Axial T1-weighted arterial phase subtraction MR image shows an enhancing liver mass (arrowheads) at the junction of segments VIII and IVa. The lesion is hyperintense to background liver on both the diffusion-weighted image (top inset, white arrow) and ADC map (bottom inset, blue arrow), which might be interpreted as T2 shine-through and fast diffusion. However, the liver is not always a useful comparator, as the background liver, in this case, is relatively hypointense (*) on the ADC map. Quantitatively, the ADC of the lesion is 1.3 mm^2/sec, compared with 2.5 mm^2/sec of the cerebrospinal fluid, indicating some degree of diffusion restriction. The results of a subsequent biopsy confirmed hepatic adenoma.

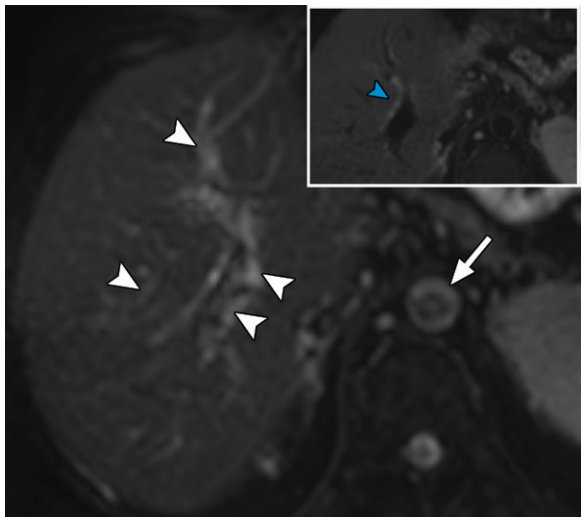

Figure 35. Effects of different low *b* values at DWI of the liver in a 58-year-old man who underwent liver MRI. Axial diffusion-weighted image with a *b* value of 0 sec/mm^2 shows heterogeneous signal intensity in the various blood vessels of the liver (white arrowheads) and the periphery of the aorta (arrow) owing to slow flow. Applying a *b* value of 50 sec/mm^2 (inset) removes vascular signal intensity, resulting in a cleaner image where the bile duct adjacent to the portal vein (blue arrowhead) is visible and background liver signal intensity is homogeneous, allowing better detection of subtle abnormalities.

at DWI is both qualitative (relative preservation of hyperintense signal with progressively higher *b* values) and quantitative (measuring the apparent diffusion coefficient [ADC] with a region of interest). The degree of diffusion restriction can be helpful in suggesting abscess in the appropriate clinical setting when there is both marked ADC hypointensity and DWI hyperintensity. The phenomenon of T2 shine-through, in which the high *b*-value image and ADC map have similar signal intensity, applies to both T2-hyperintense structures (cysts, simple fluid) and T2-hypointense structures (uterine fibroids, fibrous tissue). Thus, DWI should be interpreted in the context of the ADC map (54,55). For example, to avoid dismissing true diffusion restriction as T2 shine-through, lesional signal intensity should be compared qualitatively or quantitatively to simple fluids (eg, cerebrospinal fluid) in which fast diffusion is present (Fig 34).

DWI can also be helpful for vascular problem solving. Setting the DWI low *b* value to 50 sec/mm^2 rather than 0 sec/mm^2 removes the vascular signal in slow-flow vascular beds, normally resulting in uniform absence of vascular signal (Fig 35) (56). Vascular signal at DWI suggests thrombosis but does not distinguish bland from tumor thrombus (57). Bland thrombus restricts diffusion because of immobile water protons within the clot, whereas tumor thrombus restricts diffusion owing to tumor cells. Internal enhancement, often best appreciated at subtraction imaging owing to intrinsic T1 hyperintensity, is the key to diagnosing tumor thrombus (Fig 36) (58). Unusual enhancing structures, when lacking in DWI signal intensity, may indicate a vascular abnormality such as a pseudoaneurysm (Fig 37).

HBP Imaging

Two potential pitfalls should be recognized when interpreting HBP images. First, the signal intensity of the hepatic blood pool should be assessed. In cases of suboptimal blood pool contrast agent clearance (eg, hepatic dysfunction), the hepatic vessels can be isointense or hyperintense to the background parenchyma. As such, hemangiomas and other hypervascular lesions, which are typically HBP hypointense, may appear isointense or hyperintense owing to persistent contrast agent within their vascular spaces (ie, not because of functional hepatocytes) (Fig 38) (59).

Second, HBP liver hypointensity occurs either when hepatocytes are absent (eg, cysts or metastases) or when uptake of gadoxetate is impaired (eg, after ablation or radiation). When imaging the posttreatment liver, lesional HBP hypointensity may be misattributed to adjacent treatment effects, and correlation with other sequences is mandatory. Precontrast T1-weighted imaging serves a dual role: identifying intrinsic T1 hyperintensity within an ablation zone from coagulative necrosis, which should prompt scrutiny

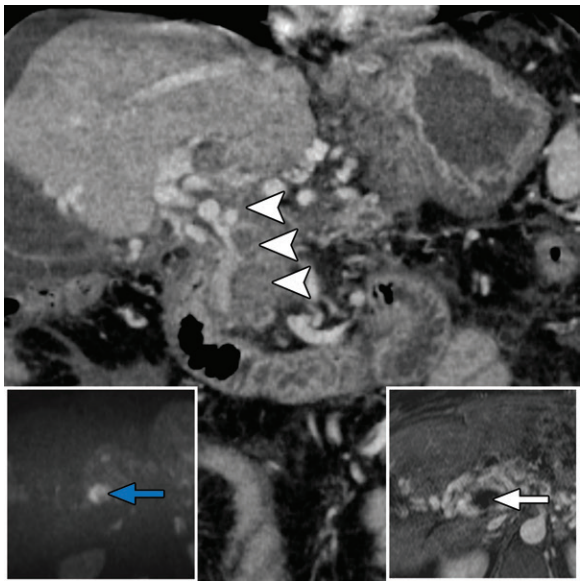

Figure 36. Thrombus evaluation with DWI in a 49-year-old man with necrotizing pancreatitis and reported portal vein tumor thrombus. Coronal contrast-enhanced CT image shows expansile soft-tissue–attenuating material (arrowheads) within the portal vein, which was interpreted as suspicious for tumor thrombus. Axial diffusion-weighted image with a *b* value of 800 sec/mm^2 (left inset) shows hyperintensity within the main portal vein (blue arrow), caused by either immobile protons within bland thrombus or dense cellularity within tumor thrombus. Axial T1-weighted portal venous phase subtraction MR image (right inset) shows nonenhancement of the portal vein (white arrow), the key finding used to distinguish bland thrombus in this case from tumor thrombus.

on subtraction and diffusion-weighted images, and identifying T1 hypointensity adjacent to an ablation zone, which should raise suspicion for disease recurrence (Fig 39) (60).

Washout

Nonperipheral washout is a major feature of HCC in LI-RADS version 2018. However, washout is not unique to HCC, nor does washout always indicate malignancy. LI-RADS characterization should only be applied in the setting of cirrhosis or other specific HCC risk factors. The imaging features of hepatic adenoma frequently overlap with those of HCC, such as nonrim APHE, nonperipheral washout, and microscopic fat (61). Consideration of patient demographics and other risk factors, such as oral contraceptive use, is crucial. Hypervascular metastases from extrahepatic primary malignancies, such as uveal melanoma and neuroendocrine tumors, also frequently exhibit washout (62) (Fig 40). The washout pattern is important, as peripheral washout is typical of adenocarcinoma, either metastatic (eg, colorectal) or primary (eg, cholangiocarcinoma) (63). Finally, washout may be difficult to perceive in a severely steatotic or siderotic liver, as both

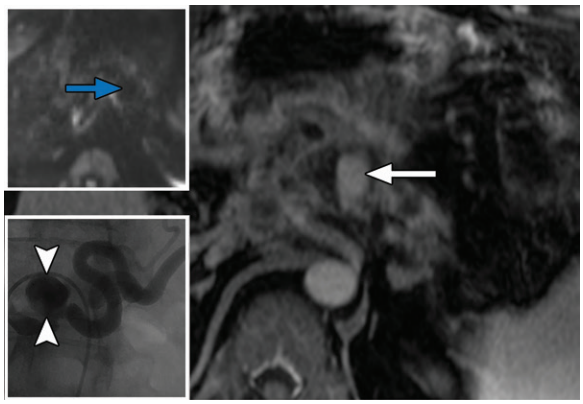

Figure 37. DWI as a vascular problem-solving tool in a 68-year-old man with pancreatic adenocarcinoma. Axial T1-weighted arterial phase MR image shows an enhancing "lesion" (white arrow) within a necrotic pancreatic mass. Diffusion-weighted image with a *b* value of 50 sec/mm^2 (top inset) shows no signal intensity (blue arrow), raising suspicion for a vascular abnormality rather than an enhancing solid mass. A splenic artery pseudoaneurysm (arrowheads) was queried and subsequently confirmed and treated at catheter angiography (bottom inset).

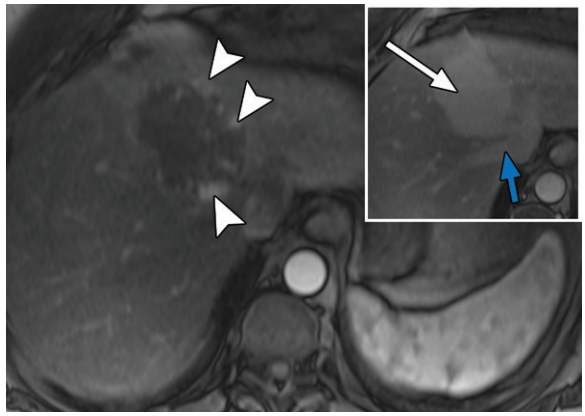

Figure 38. HBP interpretation in the context of blood pool signal intensity in a 50-year-old woman with indeterminate liver lesions. Axial T1-weighted arterial phase MR image shows peripheral nodular discontinuous APHE (arrowheads) in a segment VIII/IVa liver lesion, characteristic of a cavernous hemangioma. T1-weighted HBP image at 60 minutes with gadobenate (inset) shows diffuse hyperintensity of the mass (white arrow) compared with background liver, atypical of a hemangioma in the HBP. However, the blood pool (blue arrow) is similarly hyperintense owing to severe hepatic steatosis. The hemangioma should be recognized as following blood pool signal intensity rather than retaining contrast material with HBP imaging.

iron and fat will reduce background liver signal intensity on postcontrast T1-weighted spoiled gradient-echo images obtained with a minimal TE similar to the opposed phase.

Conclusion

As body MRI has become routine with widespread application across multiple clinical domains, general radiology practices must be equipped to perform and read these studies effectively and

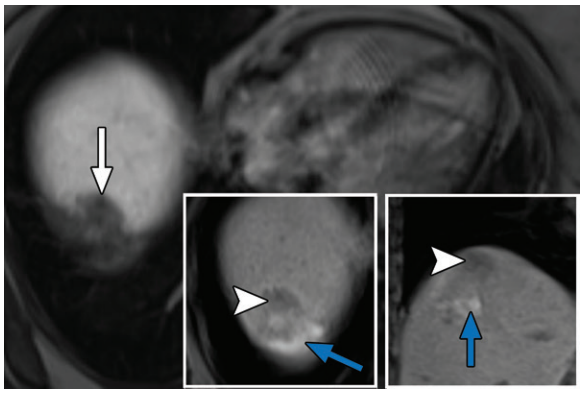

Figure 39. Postablation HBP imaging in a 56-year-old woman with metastatic rectal cancer after microwave ablation of a hepatic metastasis. Axial T1-weighted HBP image with gadoxetate shows hypointensity (white arrow) of an ablated segment VII liver dome metastasis. Nonviable ablated tissue is difficult to distinguish from viable tumor. Local recurrence can be more easily identified on the axial (left inset) and coronal (right inset) T1-weighted precontrast MR images, which show hypointensity of recurrent tumor (white arrowheads) adjacent to the intrinsically T1-hyperintense ablation zone (blue arrows).

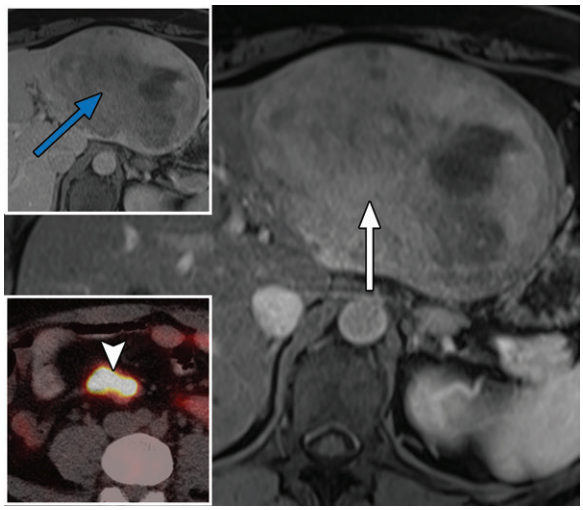

Figure 40. Washout of a liver mass in a 38-year-old woman with metastatic neuroendocrine carcinoma. Axial T1-weighted arterial phase MR image shows nonrim hyperenhancement of a large mass (white arrow) in the left lateral section of the liver, which subsequently washes out (blue arrow) on the portal venous phase image (top inset). Washout is not specific for HCC in patients without cirrhosis or other risk factors. In this patient, the mass represents a metastasis from metastatic neuroendocrine carcinoma, with a mesenteric mass (arrowhead) identified on the gallium 68 (^{68}Ga)-[tetraxetan-D-Phe1, Tyr3]-octreotate (DOTATATE) PET/CT image (bottom inset).

accurately. This article highlights key concepts in protocol design, including contrast agent selection, arterial phase timing, unique issues with gadoxetate, and the value of Dixon chemical shift imaging. We describe clinically relevant artifacts as problems and solutions and explore fat imaging. Motion artifacts and potential solutions are discussed. Finally, we present interpretive tips gleaned from our clinical experience. By bringing together these concepts into a single article, we aim to provide a reference that abdominal imagers can consult as they update body MRI protocols and refine their interpretations.

***Disclosures of conflicts of interest.*—T.J.F.** Grant to institution for research support from Siemens AG; consultant to Arterys Inc; honoraria for virtual tumor boards from PrecisCa Oncology; mediolegal case review fees from Ross Fell Casey LLP; pending patent on MRI sequence (CAPTURE). **D.H.B.** Editorial board member of *RadioGraphics*.

References

1. Glazer DI, DiPiro PJ, Shinagare AB, et al. CT and MRI Protocol Variation and Optimization at an Academic Medical Center. J Am Coll Radiol 2018;15(9):1254–1258.
2. Welle CL, Guglielmo FF, Venkatesh SK. MRI of the liver: choosing the right contrast agent. Abdom Radiol (NY) 2020;45(2):384–392.
3. CT/MRI LI-RADS v2018. https://www.acr.org/Clinical-Resources/Reporting-and-Data-Systems/LI-RADS/CT-MRI-LI-RADS-v2018. Released July 2018. Accessed January 7, 2022.
4. Well L, Weinrich JM, Adam G, Bannas P. Transient Severe Respiratory Motion Artifacts After Application of Gadoxetate Disodium: What We Currently Know. Rofo 2018;190(1):20–30.
5. Rong D, He B, Tang W, et al. Comparison of Gadobenate-Enhanced MRI and Gadoxetate-Enhanced MRI for Hepatocellular Carcinoma Detection Using LI-RADS Version 2018: A Prospective Intraindividual Randomized Study. AJR Am J Roentgenol 2022;218(4):687–698.
6. Goshima S, Kanematsu M, Watanabe H, et al. Hepatic hemangioma and metastasis: differentiation with gadoxetate disodium-enhanced 3-T MRI. AJR Am J Roentgenol 2010;195(4):941–946.
7. Morin C, Drolet S, Daigle C, et al. Additional value of gadoxetic acid-enhanced MRI to conventional extracellular gadolinium-enhanced MRI for the surgical management of colorectal and neuroendocrine liver metastases. HPB (Oxford) 2020;22(5):710–715.
8. Roux M, Pigneur F, Baranes L, et al. Differentiating focal nodular hyperplasia from hepatocellular adenoma: Is hepatobiliary phase MRI (HBP-MRI) using linear gadolinium chelates always useful? Abdom Radiol (NY) 2018;43(7):1670–1681 [Published correction appears in Abdom Radiol (NY) 2018;43(8):2212.].
9. Iyama Y, Nakaura T, Yokoyama K, et al. Comparison of the Timing of Hepatic Arterial Phase and Image Quality Using Test-Bolus and Bolus-Tracking Techniques in Gadolinium-Ethoxybenzyl-Diethylenetriamine Pentaacetic Acid-Enhanced Hepatic Dynamic Magnetic Resonance Imaging. J Comput Assist Tomogr 2017;41(4):638–643.
10. Michaely HJ, Morelli JN, Budjan J, et al. CAIPIRINHA-Dixon-TWIST (CDT)-volume-interpolated breath-hold examination (VIBE): a new technique for fast time-resolved dynamic 3-dimensional imaging of the abdomen with high spatial resolution. Invest Radiol 2013;48(8):590–597.
11. Chandarana H, Feng L, Block TK, et al. Free-breathing contrast-enhanced multiphase MRI of the liver using a combination of compressed sensing, parallel imaging, and golden-angle radial sampling. Invest Radiol 2013;48(1):10–16.
12. Harder FN, Budjan J, Nickel MD, et al. Intraindividual Comparison of Compressed Sensing-Accelerated Cartesian and Radial Arterial Phase Imaging of the Liver in an Experimental Tumor Model. Invest Radiol 2021;56(7):433–441.
13. Chang SD, Thoeni RF. Effect of T1 shortening on T2-weighted MRI sequences: comparison of hepatic mass conspicuity on images acquired before and after gadolinium enhancement. AJR Am J Roentgenol 2008;190(5):1318–1323.
14. Elster AD, Sobol WT, Hinson WH. Pseudolayering of Gd-DTPA in the urinary bladder. Radiology 1990;174(2):379–381.

15. Krinsky G, Rofsky NM, Weinreb JC. Nonspecificity of short inversion time inversion recovery (STIR) as a technique of fat suppression: pitfalls in image interpretation. AJR Am J Roentgenol 1996;166(3):523–526.
16. Ringe KI, Husarik DB, Sirlin CB, Merkle EM. Gadoxetate disodium-enhanced MRI of the liver: part 1, protocol optimization and lesion appearance in the noncirrhotic liver. AJR Am J Roentgenol 2010;195(1):13–28.
17. Gutzeit A, Binkert CA, Koh DM, et al. Evaluation of the anti-peristaltic effect of glucagon and hyoscine on the small bowel: comparison of intravenous and intramuscular drug administration. Eur Radiol 2012;22(6):1186–1194.
18. Kim S, Mussi TC, Lee LJ, Mausner EV, Cho KC, Rosenkrantz AB. Effect of flip angle for optimization of image quality of gadoxetate disodium-enhanced biliary imaging at 1.5 T. AJR Am J Roentgenol 2013;200(1):90–96.
19. Matoori S, Froehlich JM, Breitenstein S, et al. Serum albumin, total bilirubin, and patient age are independent confounders of hepatobiliary-phase gadoxetate parenchymal liver enhancement. Eur Radiol 2019;29(11):5813–5822.
20. Cieszanowski A, Stadnik A, Lezak A, et al. Detection of active bile leak with Gd-EOB-DTPA enhanced MR cholangiography: comparison of 20-25 min delayed and 60-180 min delayed images. Eur J Radiol 2013;82(12):2176–2182.
21. Guglielmo FF, Mitchell DG, Roth CG, Deshmukh S. Hepatic MR imaging techniques, optimization, and artifacts. Magn Reson Imaging Clin N Am 2014;22(3):263–282.
22. Shetty AS, Sipe AL, Zulfiqar M, et al. In-Phase and Opposed-Phase Imaging: Applications of Chemical Shift and Magnetic Susceptibility in the Chest and Abdomen. RadioGraphics 2019;39(1):115–135.
23. Labranche R, Gilbert G, Cerny M, et al. Liver Iron Quantification with MR Imaging: A Primer for Radiologists. RadioGraphics 2018;38(2):392–412.
24. Newatia A, Khatri G, Friedman B, Hines J. Subtraction imaging: applications for nonvascular abdominal MRI. AJR Am J Roentgenol 2007;188(4):1018–1025.
25. Colagrande S, Centi N, Galdiero R, Ragozzino A. Transient hepatic intensity differences: part 1—Those associated with focal lesions. AJR Am J Roentgenol 2007;188(1):154–159.
26. Yanasak NE, Kelly MJ. MR imaging artifacts and parallel imaging techniques with calibration scanning: a new twist on old problems. RadioGraphics 2014;34(2):532–548.
27. Idilman IS, Ozdeniz I, Karcaaltincaba M. Hepatic Steatosis: Etiology, Patterns, and Quantification. Semin Ultrasound CT MR 2016;37(6):501–510.
28. Thomas AJ, Menias CO, Pickhardt PJ, et al. Bleeding Liver Masses: Imaging Features With Pathologic Correlation and Impact on Management. AJR Am J Roentgenol 2019;213(1):8–16.
29. Kühn JP, Berthold F, Mayerle J, et al. Pancreatic Steatosis Demonstrated at MR Imaging in the General Population: Clinical Relevance. Radiology 2015;276(1):129–136.
30. Coulier B. Pancreatic Lipomatosis: An Extensive Pictorial Review. J Belg Soc Radiol 2016;100(1):39.
31. Del Grande F, Santini F, Herzka DA, et al. Fat-suppression techniques for 3-T MR imaging of the musculoskeletal system. RadioGraphics 2014;34(1):217–233.
32. Gaddikeri S, Mossa-Basha M, Andre JB, Hippe DS, Anzai Y. Optimal Fat Suppression in Head and Neck MRI: Comparison of Multipoint Dixon with 2 Different Fat-Suppression Techniques, Spectral Presaturation and Inversion Recovery, and STIR. AJNR Am J Neuroradiol 2018;39(2):362–368.
33. van Vucht N, Santiago R, Lottmann B, et al. The Dixon technique for MRI of the bone marrow. Skeletal Radiol 2019;48(12):1861–1874.
34. Maeder Y, Dunet V, Richard R, Becce F, Omoumi P. Bone Marrow Metastases: T2-weighted Dixon Spin-Echo Fat Images Can Replace T1-weighted Spin-Echo Images. Radiology 2018;286(3):948–959.
35. Ji X, Huang W, Dong H, et al. Evaluation of bone marrow infiltration in multiple myeloma using whole-body diffusion-weighted imaging and T1-weighted water-fat separation Dixon. Quant Imaging Med Surg 2021;11(2):641–651.
36. Schieda N, Davenport MS, Pedrosa I, et al. Renal and adrenal masses containing fat at MRI: Proposed nomenclature by the society of abdominal radiology disease-focused panel on renal cell carcinoma. J Magn Reson Imaging 2019;49(4):917–926.
37. Yousaf A, Nabi U, Hussein ML, Twair A, Gashir MB. Fat-Containing Renal Cell Carcinoma Mimicking Angiomyolipoma: A Radiological and Histopathological Diagnostic Challenge. Cureus 2020;12(1):e6721.
38. Curry NS, Schabel SI, Garvin AJ, Fish G. Intratumoral fat in a renal oncocytoma mimicking angiomyolipoma. AJR Am J Roentgenol 1990;154(2):307–308.
39. Pedrosa I, Cadeddu JA. How We Do It: Managing the Indeterminate Renal Mass with the MRI Clear Cell Likelihood Score. Radiology 2022;302(2):256–269.
40. Hakim SW, Schieda N, Hodgdon T, McInnes MDF, Dilauro M, Flood TA. Angiomyolipoma (AML) without visible fat: Ultrasound, CT and MR imaging features with pathological correlation. Eur Radiol 2016;26(2):592–600.
41. Woo S, Cho JY, Kim SY, Kim SH. Adrenal adenoma and metastasis from clear cell renal cell carcinoma: can they be differentiated using standard MR techniques? Acta Radiol 2014;55(9):1120–1128.
42. Schieda N, Siegelman ES. Update on CT and MRI of Adrenal Nodules. AJR Am J Roentgenol 2017;208(6):1206–1217.
43. Sung CT, Shetty A, Menias CO, et al. Collision and composite tumors; radiologic and pathologic correlation. Abdom Radiol (NY) 2017;42(12):2909–2926.
44. Huang SY, Seethamraju RT, Patel P, Hahn PF, Kirsch JE, Guimaraes AR. Body MR Imaging: Artifacts, k-Space, and Solutions. RadioGraphics 2015;35(5):1439–1460.
45. Kozak BM, Jaimes C, Kirsch J, Gee MS. MRI Techniques to Decrease Imaging Times in Children. RadioGraphics 2020;40(2):485–502.
46. Tokoro H, Yamada A, Suzuki T, et al. Usefulness of breath-hold compressed sensing accelerated three-dimensional magnetic resonance cholangiopancreatography (MRCP) added to respiratory-gating conventional MRCP. Eur J Radiol 2020;122:108765.
47. Lee JH, Choi YH, Cheon JE, et al. Improved abdominal MRI in non-breath-holding children using a radial k-space sampling technique. Pediatr Radiol 2015;45(6):840–846.
48. Duffy PB, Stemmer A, Callahan MJ, et al. Free-breathing radial stack-of-stars three-dimensional Dixon gradient echo sequence in abdominal magnetic resonance imaging in sedated pediatric patients. Pediatr Radiol 2021;51(9):1645–1653.
49. Rosenkrantz AB, Patel JM, Babb JS, Storey P, Hecht EM. Liver MRI at 3 T using a respiratory-triggered time-efficient 3D T2-weighted technique: impact on artifacts and image quality. AJR Am J Roentgenol 2010;194(3):634–641.
50. Kandpal H, Sharma R, Madhusudhan KS, Kapoor KS. Respiratory-triggered versus breath-hold diffusion-weighted MRI of liver lesions: comparison of image quality and apparent diffusion coefficient values. AJR Am J Roentgenol 2009;192(4):915–922.
51. Moore WA, Khatri G, Madhuranthakam AJ, Sims RD, Pedrosa I. Added value of diffusion-weighted acquisitions in MRI of the abdomen and pelvis. AJR Am J Roentgenol 2014;202(5):995–1006.
52. Morani AC, Elsayes KM, Liu PS, et al. Abdominal applications of diffusion-weighted magnetic resonance imaging: Where do we stand. World J Radiol 2013;5(3):68–80.
53. Dunn DP, Lee KS, Smith MP, Mortele KJ. Nononcologic applications of diffusion-weighted imaging in the gastrointestinal system. AJR Am J Roentgenol 2015;204(4):758–767.
54. Malayeri AA, El Khouli RH, Zaheer A, et al. Principles and applications of diffusion-weighted imaging in cancer detection, staging, and treatment follow-up. RadioGraphics 2011;31(6):1773–1791.
55. Baliyan V, Das CJ, Sharma R, Gupta AK. Diffusion weighted imaging: Technique and applications. World J Radiol 2016;8(9):785–798.
56. Qayyum A. Diffusion-weighted imaging in the abdomen and pelvis: concepts and applications. RadioGraphics 2009;29(6):1797–1810.

57. Ahn JH, Yu JS, Cho ES, Chung JJ, Kim JH, Kim KW. Diffusion-Weighted MRI of Malignant versus Benign Portal Vein Thrombosis. Korean J Radiol 2016;17(4):533–540.
58. Sherman CB, Behr S, Dodge JL, Roberts JP, Yao FY, Mehta N. Distinguishing Tumor From Bland Portal Vein Thrombus in Liver Transplant Candidates With Hepatocellular Carcinoma: the A-VENA Criteria. Liver Transpl 2019;25(2):207–216.
59. Fu GL, Du Y, Zee CS, et al. Gadobenate dimeglumine-enhanced liver magnetic resonance imaging: value of hepatobiliary phase for the detection of focal liver lesions. J Comput Assist Tomogr 2012;36(1):14–19.
60. Furlan A, Marin D, Bae KT, et al. Focal liver lesions hyperintense on T1-weighted magnetic resonance images. Semin Ultrasound CT MR 2009;30(5):436–449.
61. Grazioli L, Bondioni MP, Haradome H, et al. Hepatocellular adenoma and focal nodular hyperplasia: value of gadoxetic acid-enhanced MR imaging in differential diagnosis. Radiology 2012;262(2):520–529.
62. Namasivayam S, Martin DR, Saini S. Imaging of liver metastases: MRI. Cancer Imaging 2007;7(1):2–9.
63. Mamone G, Miraglia R. The "peripheral wash-out sign" in hepatic malignant lesions. Abdom Radiol (NY) 2019;44(8):2937–2938.